

***E. coli* do not count single molecules**

Henry H. Mattingly^{†,1}, Keita Kamino^{†,2}, Jude Ong^{‡,3}, Rafaela Kottou^{‡,3}, Thierry Emonet^{*,3,4,5}, Benjamin B. Machta^{*,4,5}

¹ Center for Computational Biology, Flatiron Institute

² Institute of Molecular Biology, Academia Sinica

³ Molecular, Cellular, and Developmental Biology, ⁴ Physics, and ⁵ QBio Institute, Yale University

† These authors contributed equally.

‡ These authors contributed equally.

* Correspondence to: Benjamin.machta@yale.edu and Thierry.emonet@yale.edu.

Abstract

Organisms must perform sensory-motor behaviors to survive. What bounds or constraints limit behavioral performance? Previously, we found that the gradient-climbing speed of a chemotaxing *Escherichia coli* is near a bound set by the limited information they acquire from their chemical environments (1). Here we ask what limits their sensory accuracy. Past theoretical analyses have shown that the stochasticity of single molecule arrivals sets a fundamental limit on the precision of chemical sensing (2). Although it has been argued that bacteria approach this limit, direct evidence is lacking. Here, using information theory and quantitative experiments, we find that *E. coli*'s chemosensing is *not* limited by the physics of particle counting. First, we derive the physical limit on the behaviorally-relevant information that any sensor can get about a changing chemical concentration, assuming that every molecule arriving at the sensor is recorded. Then, we derive and measure how much information *E. coli*'s signaling pathway encodes during chemotaxis. We find that *E. coli* encode two orders of magnitude less information than an ideal sensor limited only by shot noise in particle arrivals. These results strongly suggest that constraints other than particle arrival noise limit *E. coli*'s sensory fidelity.

Introduction

Organisms must rapidly and accurately sense their environment, and then act on that sensory information to perform motor behaviors. Despite the importance of these processes for organisms' survival, it is unclear what factors limit sensory fidelity and how this fidelity impacts behavioral performance (3). Past works have demonstrated that physics external to an organism often place fundamental limits on sensing accuracy and have argued that biological sensory systems might approach these limits (4,5,2,6–9). Alternatively, it is possible that other, system-specific constraints combined with demands on cellular resources are instead limiting (10–17). Understanding which constituent processes of a behavior limit performance would reveal relevant constraints on evolution and learning of sensory-motor behaviors.

Escherichia coli chemotaxis is an ideal system to study these questions. Bacteria use the chemotaxis system to navigate chemical gradients, which is important for fitness-relevant behaviors such as climbing quickly or localizing at sources (18–21). Furthermore, we understand in detail how *E. coli* sense and act on chemical signals (22–24). *E. coli* alternate between straight-swimming runs and randomly-reorienting

tumbles (25). As they swim, the local concentrations of attractant chemicals change in time. These extracellular ligands bind to the cell's transmembrane receptors, which modify the activity of receptor-associated CheA kinases inside the cell. CheA phosphorylates the diffusible response regulator CheY, which is dephosphorylated by CheZ. When conditions worsen, kinase activity increases, increasing CheYp concentration. CheYp then binds to the motor and increases the propensity to tumble, biasing the cell's runs towards more favorable chemical environments.

We recently demonstrated that *E. coli* chemotaxis is information-limited: cells climb shallow gradients near a bound set by their sensory capabilities (1). First, we showed theoretically that the rate at which a cell encodes information about chemical signals sets an upper limit on its gradient-climbing speed. Then, through a combination of single-cell Förster resonance energy transfer (FRET) experiments and measurements of cells swimming in gradients, we found that a typical *E. coli* cell gets very little information—about 0.01 bits/s in a centimeter-long gradient—but efficiently uses this information to climb gradients at speeds near the theoretical limit. This suggests that a bacterium with a more accurate sensor would climb gradients faster, likely increasing their fitness.

What prevents *E. coli* from obtaining more information during chemotaxis? In their classic work, Berg and Purcell demonstrated that the stochastic arrival of particles at the cell surface places a fundamental limit on the accuracy of chemical sensing (2), regardless of its sensor's molecular details. Since then, theoretical works have studied the effects of receptor binding (26–28), maximum-likelihood estimation (29), energy consumption with noisy readout molecules (10,30–32), time-varying concentrations (11,33,34), constant concentration ramps (8,35,36), and other factors (28,37) on this fundamental limit. Furthermore, several studies have argued that the sensitivity of bacteria's chemosensing apparatus approaches the molecule-counting limit (2,8). However, it is still unclear whether this fundamental limit meaningfully constrains the information *E. coli* get about chemical signals, and thus their speed at climbing gradients. Answering this question has been challenging because it has been unclear how the fidelity of chemosensing relates to chemotaxis performance, and because of difficulties with measuring, quantifying, and interpreting cells' internal encoding of external signals.

Here, we address these challenges with a combination of information theory and single-cell FRET measurements. Information theory allows us to quantify the fidelity of signal encoding in a cellular system, and single-cell FRET measurements give us a direct readout of the kinase activity in which *E. coli* encode environmental information. We first derive the physical limit on the rate at which an ideal sensor can acquire behaviorally-relevant information, set by ligand arrival noise. Next, we derive the rate at which *E. coli* encode this information in their kinase activity. By measuring signal statistics, kinase response functions, and fluctuations in kinase activity, we quantify both the physical limit and how much information a typical *E. coli* cell gets during chemotaxis. We find that *E. coli* get orders of magnitude less information than the physical limit. Therefore, when signals are weak and sensor quality matters, cells climb gradients much slower than an ideal, single-molecule-sensing agent could. Our work opens up new questions about what costs, constraints, or competing objectives prevent them from being closer to the physical limit.

Chemotaxis requires information about the current time derivative of concentration

Determining whether particle arrival noise is a limiting factor during *E. coli* chemotaxis presents conceptual challenges. Cells process measurements of their chemical environment into internal states, like the activity of kinases and the concentrations of signaling molecules. However, the goal of the chemotaxis system is not to represent the current concentration with high accuracy per se, but instead to utilize the concentration signal to move up a chemical gradient. Thus, cells need to capture certain aspects of signals that are behaviorally-relevant, but not necessarily in a format which is simply interpretable to an observer. To quantify how accurate such internal representations are thus requires a mathematical understanding of what features of the concentration signal are relevant to chemotaxis.

Our approach for addressing this builds on our recent work (1), where we identified the behaviorally-relevant information for *E. coli* chemotaxis. In particular, we showed that the amount of such information that the cell uses at the motor *determines* its gradient-climbing speed, $v_d \propto (i)^{1/2}$. Furthermore, due to the data-processing inequality (38,39), the amount of this information in any intermediate variable *bounds* performance (see also SI). The key chemical signal that the cell needs to encode is the (relative) rate of change of concentration, $s(t) = \frac{d}{dt} \log(c)$ (Fig. 1). Then, the behaviorally-relevant information is the “transfer entropy rate” (40) from *current* signal, $s(t)$, to a time-dependent variable $x(t)$ that encodes the signal in its trajectory, $\{x\}$, up to time t :

$$\dot{I}_{s \rightarrow x}^* \equiv \lim_{dt \rightarrow 0} \frac{1}{dt} I(x(t+dt); s(t) | \{x\}), \quad (1)$$

where $I(X; Y | Z)$ is the mutual information between X and Y , conditioned on Z (38,41). Importantly, the current value of $x(t)$ does not need to be an explicit representation of $s(t)$; it just has to carry information about $s(t)$ in its trajectory.

This points to a way of quantifying how molecule-counting noise limits behaviorally-relevant information for chemotaxis, and how *E. coli* compare to the limit. The stochastic arrival rate of ligand molecules at the cell surface, $r(t)$, is the first quantity that a cell can physically measure that encodes information about signals $s(t)$ (Fig. 1). Thus, the transfer entropy rate $\dot{I}_{s \rightarrow r}^*$ (i.e. with $x = r$ in Eqn. 1) is a fundamental physical limit on the sensory information available for chemotaxis. An ideal agent would make navigation decisions based on a perfect readout of past particle arrivals $\{r\}$, but this process would still be noisy due to their inherent stochasticity. Then, *E. coli* encodes the signal in the activity of CheA kinases, $\{a\}$, from which downstream behavioral decisions are made. The data-processing inequality implies that $\dot{I}_{s \rightarrow r}^* \geq \dot{I}_{s \rightarrow a}^*$. Therefore, to compare *E. coli* to the physical limit, we must quantify the information about $s(t)$ encoded in $\{a\}$, $\dot{I}_{s \rightarrow a}^*$ (i.e. with $x = a$ in Eqn. 1). If $\dot{I}_{s \rightarrow a}^*$ is comparable to $\dot{I}_{s \rightarrow r}^*$, then *E. coli*'s signaling pathway acquires most of the information that is available in molecule arrivals. This comparison would allow us to determine whether *E. coli*'s chemotaxis performance is limited by the external physics of ligand diffusion or by other factors.

Our task now is to obtain closed form expressions for $\dot{I}_{s \rightarrow r}^*$ and $\dot{I}_{s \rightarrow a}^*$, and then quantify them with experimental measurements. In the SI (Eqn. 10), we show that this transfer entropy rate is equivalent to a *predictive* information rate (42–48),

$$\dot{I}_{s \rightarrow x}^* = -[\partial_\tau I(s(t+\tau); \{x\})]_{\tau=0}. \quad (2)$$

On the right, τ is a time interval into the future at which the signal $s(t+\tau)$ is predicted from past observations, $\{x\}$, making this a predictive information. Thus, the information about current signal $s(t)$

that is *encoded* in past x is the same as the accuracy with which $s(t)$ can be *estimated* from past x . We used this form to derive expressions for $\dot{I}_{s \rightarrow r}^*$ and $\dot{I}_{s \rightarrow a}^*$ (SI). Fig. 1 illustrates this problem, showing simulated time traces of signal s , particle arrival rate r , and kinase activity a . The goal of a chemotaxing *E. coli* is to construct an optimal running estimate of $s(t)$. An ideal agent does this from observations $\{r\}$, whereas the cell only has access to past kinase activity $\{a\}$.

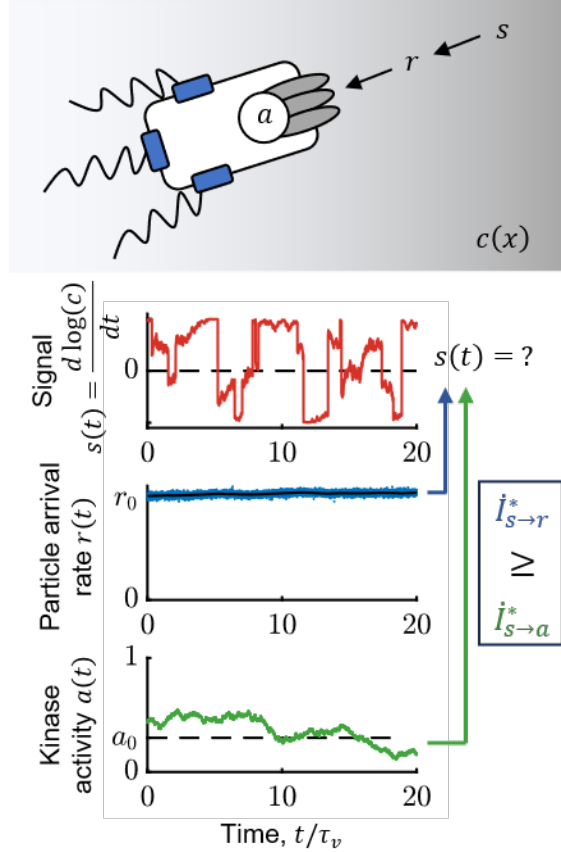


Figure 1: *E. coli* need to infer rate of change of attractant concentration from stochastic molecule arrivals. Top: Bacteria do not measure signal $s = \frac{d}{dt} \log(c)$ directly—instead, they can at best measure stochastic particle arrivals at rate $r(t)$ at their transmembrane receptors. Receptor-associated kinases respond to ligand arrivals with changes in activity, $a(t)$, and encode information about $s(t)$, but also introduce additional noise. Bottom: Simulated traces of $s(t)$ (red); $r(t)$ (blue); $\langle r(t) \rangle = k_D c(t)$ (black); and kinase activity $a(t)$ (green) for a cell exhibiting run-and-tumble motion in a shallow chemical gradient. r_0 is the background particle arrival rate, $r_0 = k_D c_0$, and a_0 is the baseline level of kinase activity. The cell’s task is to infer $s(t)$ from kinase activity a , and the fidelity of this inference is quantified by the transfer entropy rate, $\dot{I}_{s \rightarrow a}^*$. An ideal agent would directly estimate $s(t)$ from the particle arrival rate r , without the noise in kinase activity, thus setting the physical limit, $\dot{I}_{s \rightarrow r}^*$. The simulation above was performed in a background concentration $c_0 = 1 \mu\text{M}$ and gradient of steepness $g = 0.3 \text{ mm}^{-1}$.

Physical limit on information due to stochastic particle arrivals

We first derive an expression for the physical limit, $\dot{I}_{s \rightarrow r}^*$, from a model for the dynamics of $s(t)$ and $r(t)$. In static gradients, the signals a cell experiences are determined by their own motion in the gradient. Accordingly, in a gradient of steepness $g = d \log(c) / dx$, the signal is $s(t) = g v_x(t)$, where v_x is the cell's up-gradient velocity. As done previously (1,48), we consider a cell exhibiting run-and-tumble motion in a shallow gradient. In this regime, to leading order in g , the information rate only depends on the correlation function of up-gradient velocity in the absence of a gradient, $V(t)$, since s is proportional to g . Thus, we approximate the signal as Gaussian, and its dynamics are fully characterized by the following correlation function:

$$\langle s(t) s(t') \rangle = g^2 V(t - t') = g^2 \sigma_v^2 \exp\left(-\frac{|t - t'|}{\tau_v}\right). \quad (3)$$

Here, $V(t)$ is the correlation function of v_x , σ_v^2 is the variance v_x , and τ_v is the signal correlation time, which depends on the cell's mean run duration, the persistence of tumbles, and rotational diffusion (1,49).

We take particle arrival events to follow a Poisson process with time-varying rate $\langle r(t) \rangle = 4 D l c(t) = k_D c(t)$, where D is the diffusivity of the ligand and l is the diameter of a circular patch on the cell's surface (2,28). If a sufficient number of particles arrive per run, $r_0 \tau_v \gg 1$, which is valid in our experimental conditions, we can approximate the number of particles that arrive per unit time as Gaussian:

$$r(t) = k_D c(t) + \sqrt{r_0} \xi(t). \quad (4)$$

Here, $r_0 = k_D c_0$ is the background molecule arrival rate, where c_0 is the background concentration, and the noise is $\langle \xi(t) \xi(t') \rangle = \delta(t - t')$.

Next, since $s(t)$ and $\{r\}$ are each approximately Gaussian, the mutual information between them in Eqn. 2 has a known form (38) (SI Eqn. 13). In particular, it depends on $\sigma_{s|r}^2(\tau)$, the variance of the optimal estimate of $s(t + \tau)$ constructed from the past of r . Thus, the problem of deriving the physical limit reduces to solving $\sigma_{s|r}^2(\tau)$, which can be done using causal Wiener filtering theory (50–52) (see also (44,48,53–55)) (SI). In the SI, we derive the physical limit on behaviorally-relevant information for chemotaxis, which in the limit of shallow gradients reduces to:

$$\dot{I}_{s \rightarrow r}^* \approx \frac{1}{\tau_v} \frac{1}{4} \gamma_r. \quad (5)$$

Above, we have defined the dimensionless signal-to-noise ratio of particle arrivals, $\gamma_r = 2 r_0 g^2 \sigma_v^2 \tau_v^3$. Eqn. 5 is valid when $\gamma_r \ll 1$, which defines the small-signal regime for $\dot{I}_{s \rightarrow r}^*$. We also provide a full expression for $\dot{I}_{s \rightarrow r}^*$ in the SI (Eqn. 44). The signal strength is proportional to r_0^2 , while the noise is proportional to r_0 . Thus, increasing the molecular arrival rate r_0 , the gradient steepness g , or the variance of the up-gradient swimming speed σ_v increases the signal-to-noise ratio of particle arrivals. Furthermore, the longer the cell maintains its heading, τ_v , the more time it has to average out the noise of particle arrivals. Past work has shown that the relative error of estimating a constant time derivative scales as $1/T^3$, where T is the integration time (35). In chemotaxis, the longest reasonable integration time is the time scale on which the signal doesn't change significantly, τ_v . Therefore, a factor of τ_v^3 appears in γ_r . The derivation of $\dot{I}_{s \rightarrow r}^*$ also provides the optimal kernel for constructing a running estimate of $s(t)$ given past particle arrivals $\{r\}$, which we discuss in the SI (Fig. S4).

Above, we have modeled an ideal sensor that “absorbs” every molecule it senses (2). If the sensor cannot distinguish between new ligand arrival events and rebinding events, the bound is lower by an order-1 prefactor (28,37).

Information encoded in *E. coli*'s CheA kinase activity

How do *E. coli* compare to the fundamental limit? To answer this, we need to derive and experimentally quantify the information, $I_{s \rightarrow a}^*$, encoded in the activity $a(t)$ of *E. coli*'s CheA kinases. This in turn requires models for both noise and responses of kinase activity.

As done before (1), in shallow gradients or for small signals, kinase activity can be described using linear response theory. In background particle arrival rate r_0 and with steady-state kinase activity a_0 , then activity becomes:

$$a(t) = a_0 - \int_{-\infty}^t K_r(t-t') (r(t') - r_0) dt' + \eta_n(t). \quad (6)$$

E. coli respond to a step increase in attractant concentration with a fast initial drop in kinase activity, followed by slow adaptation back to pre-stimulus levels (56). This response is captured by a phenomenological form for the response function:

$$K_r(t) = G_r \left(\left(\frac{1}{\tau_1} + \frac{1}{\tau_2} \right) \exp \left(- \left(\frac{1}{\tau_1} + \frac{1}{\tau_2} \right) t \right) - \frac{1}{\tau_2} \exp \left(- \frac{t}{\tau_2} \right) \right) \Theta(t), \quad (7)$$

where G_r is the gain of the response to particle arrival rate r , τ_1 is the fast initial response time, τ_2 is the slow adaptation time, and $\Theta(t)$ is the Heaviside step function. This response function can equivalently be expressed in terms of responses to past signals s , with a related kernel $K(t)$ that we used previously (1) ($K_r(t) = \frac{1}{r_0} \frac{d}{dt} K(t)$; Methods, Eqn. 15 below).

Noise in kinase activity is driven by a combination of stochastic particle arrivals and internally-driven fluctuations. Single-cell experiments have observed large, slow fluctuations in kinase activity on a time scale of 10 s (1,57–59). These are well-described as Gaussian, $\eta_n(t)$ in Eqn. 6, with correlation function:

$$\langle \eta_n(t) \eta_n(t') \rangle = D_n \tau_n \exp \left(- \frac{|t-t'|}{\tau_n} \right). \quad (8)$$

Here, D_n is the diffusivity of slow noise in kinase activity, and τ_n is its correlation time. So far, it has not been possible to measure noise in kinase activity at time scales near or below τ_1 , but the noise cannot go below the level set by kinase responses to particle arrival noise. Thus, we construct a phenomenological noise model that agrees with experiments at low frequencies while obeying known physics at high frequencies. This consists of adding kinase responses to particle shot noise in Eqn. 4 to the slow fluctuations in Eqn. 8. Due to the adaptive nature of the signaling pathway, all the parameters that appear in the above Eqns. 7 and 8 can depend on the background particle arrival rate, r_0 .

With this model, we can derive an expression for the information about signal encoded in kinase activity, $I_{s \rightarrow a}^*$. As above, this reduces to deriving $\sigma_{s|a}^2(\tau)$, the variance of the signal $s(t+\tau)$ reconstructed from the past of kinase activity $\{a\}$, which can again be solved using Wiener filtering theory (SI). Furthermore,

previous measurements (and measurements below) have shown that $\tau_1 \ll \tau_v$ (1,60,61) and $\tau_2 \approx \tau_n$ (1). Thus, in shallow gradients, we find that the information rate to kinase activity is:

$$\dot{I}_{S \rightarrow a}^* \approx \frac{1}{\tau_v} \frac{1}{4} \gamma_a \frac{\gamma_r / \gamma_a}{(1 + \sqrt{\gamma_r / \gamma_a})^2}. \quad (9)$$

Here, we have defined the dimensionless kinase signal-to-noise ratio $\gamma_a = \frac{G_r^2}{D_n} r_0^2 g^2 \sigma_v^2 \tau_v$ and used $\gamma_r = 2 r_0 g^2 \sigma_v^2 \tau_v^3$ from above. Eqn. 9 is valid when $\gamma_a \ll 1$, which defines the small-signal regime for $\dot{I}_{S \rightarrow a}^*$. We also provide a full expression for $\dot{I}_{S \rightarrow a}^*$ in the SI (Eqn. 89). An ideal cell with no internal noise sources would operate at the physical limit, Eqn. 5, corresponding to infinite signal-to-noise in kinase activity, $\gamma_a \rightarrow \infty$. Taking this limit in Eqn. 9 results in the expression for $\dot{I}_{S \rightarrow r}^*$ above (Eqn. 5). Conversely, a cell with internal noise would degrade information about the signal, and in the limit of large noise would have an information rate given by $\dot{I}_{S \rightarrow a}^* \approx \frac{1}{\tau_v} \frac{1}{4} \gamma_a$. The derivation of $\dot{I}_{S \rightarrow a}^*$ also provides the optimal kernel for constructing a running estimate of $s(t)$ from past kinase activity $\{a\}$, which we discuss in the SI.

To compare the information *E. coli* get during chemotaxis to the physical limit, we must quantify $\dot{I}_{S \rightarrow a}^*$ and $\dot{I}_{S \rightarrow r}^*$ by measuring the parameters above from live cells.

Single-cell measurements constrain signal and kinase properties

Next, we use single-cell tracking and FRET experiments to measure the parameters that characterize the signal statistics, kinase response function, and kinase noise statistics in multiple background concentrations of attractant. As the attractant, we used aspartate (Asp), to which the *E. coli* chemotaxis signaling pathway responds with the highest sensitivity among known attractants (62).

To quantify the parameters describing cell swimming statistics (Eqn. 3), and thus the signal statistics, σ_v^2 and τ_v , we recorded trajectories of cells swimming in multiple uniform background concentrations of Asp: $c_0 = 0.1, 1, \text{ and } 10 \mu\text{M}$ (Fig. 2A). Single cells in the clonal population exhibited a range of swimming behaviors (57,63–69); thus, as before (1), we focus on cells with median values of the phenotypic parameters. We binned cells by the fraction of time they spent in the “run” state, P_{run} , and computed the velocity correlation function, $V(t)$, among cells with the median P_{run} . The parameters σ_v^2 and τ_v in each background c_0 were then inferred by fitting the correlation functions with the decaying exponential in Eqn. 3. These parameters depended weakly on c_0 , and their values in $c_0 = 1 \mu\text{M}$ Asp were $\sigma_v^2 = 146 \pm 5 (\mu\text{m/s})^2$ and $\tau_v = 1.19 \pm 0.01 \text{ s}$ (see Fig. S1AB for their values in all backgrounds).

We measured kinase response functions as before (1), using a microfluidic device in which we can deliver controlled chemical stimuli with high time resolution ($\sim 100 \text{ ms}$) (70). Cells immobilized in the device were delivered ten small positive and negative step changes of Asp concentration around multiple backgrounds c_0 (Fig. 2B; Methods). Kinase responses were measured in single cells through FRET (58,59,70–74) between CheZ-mYFP and CheY-mRFP. Then we fit each cell’s average response with the phenomenological response function $K_r(t)$ in Eqn. 7, and computed the population-median parameter values. However, τ_1 estimated this way includes the dynamics of CheY-CheZ interactions, which are slower than the fast time scale of the kinases. We used $\tau_1 = 0$ for calculations below, which slightly overestimates the information rate $\dot{I}_{S \rightarrow a}^*$, making this a conservative choice in estimating where cells are relative to the bound. The

adaptation time τ_2 depended weakly on c_0 (in $c_0 = 1 \mu\text{M}$, $\tau_2 = 7.4 \pm 0.3 \text{ s}$) (Fig. S1D), but G_r varied significantly with c_0 : for $c_0 = \{0.1, 1, 10\} \mu\text{M}$ we measured $G_r = \frac{1}{kD} \{3.2 \pm 0.1, 2.28 \pm 0.05, 0.251 \pm 0.009\}$ (Fig. S1EF).

The dependence of G_r on c_0 was consistent with the phenomenological Monod-Wyman-Changeux (MWC) model for kinase activity (23,75–77), which captures numerous experimental measurements (70,72–74,78). First, in the methods we note that $G_r = \frac{1}{r_0} G(c_0)$, where $G(c_0)$ is the MWC model gain (Eqn. 16 in the Methods below). The MWC model in turn predicts that $G(c_0) \approx G_\infty \frac{c_0}{c_0 + K_i}$, where K_i is the dissociation constant of two-state receptors for ligand when in their inactive state and G_∞ is a constant (Methods). Thus, in low backgrounds where $c_0 \ll K_i$ the cell is in the “linear-sensing” regime and $G_r = G_\infty \frac{1}{k_D K_i}$ is constant; in high backgrounds where $c_0 \gg K_i$, cells transition to the “log-sensing” regime (79–81), with gain $G_r \approx G_\infty / r_0$. Fitting $G(c_0)$ to the MWC model, we estimated that $G_\infty = 3.5 \pm 0.1$ and $K_i = 0.81 \pm 0.04 \mu\text{M}$.

Finally, we estimated the noise parameters of slow kinase fluctuations by measuring kinase activity in single cells experiencing constant Asp concentrations c_0 (Fig. 2C). The diffusivity D_n and time scale τ_n of slow fluctuations in Eqn. 8 were extracted from these time series using Bayesian filtering (1,82) (Methods). We then computed the population-median parameter values. Both of these parameters depended weakly on c_0 , and their values in $c_0 = 1 \mu\text{M}$ were $D_n = 8.1 \pm 0.9 \times 10^{-4} \text{ s}^{-1}$ and $\tau_n = 8.7 \pm 0.9 \text{ s}$ (see Fig. S1CD for their values in all backgrounds).

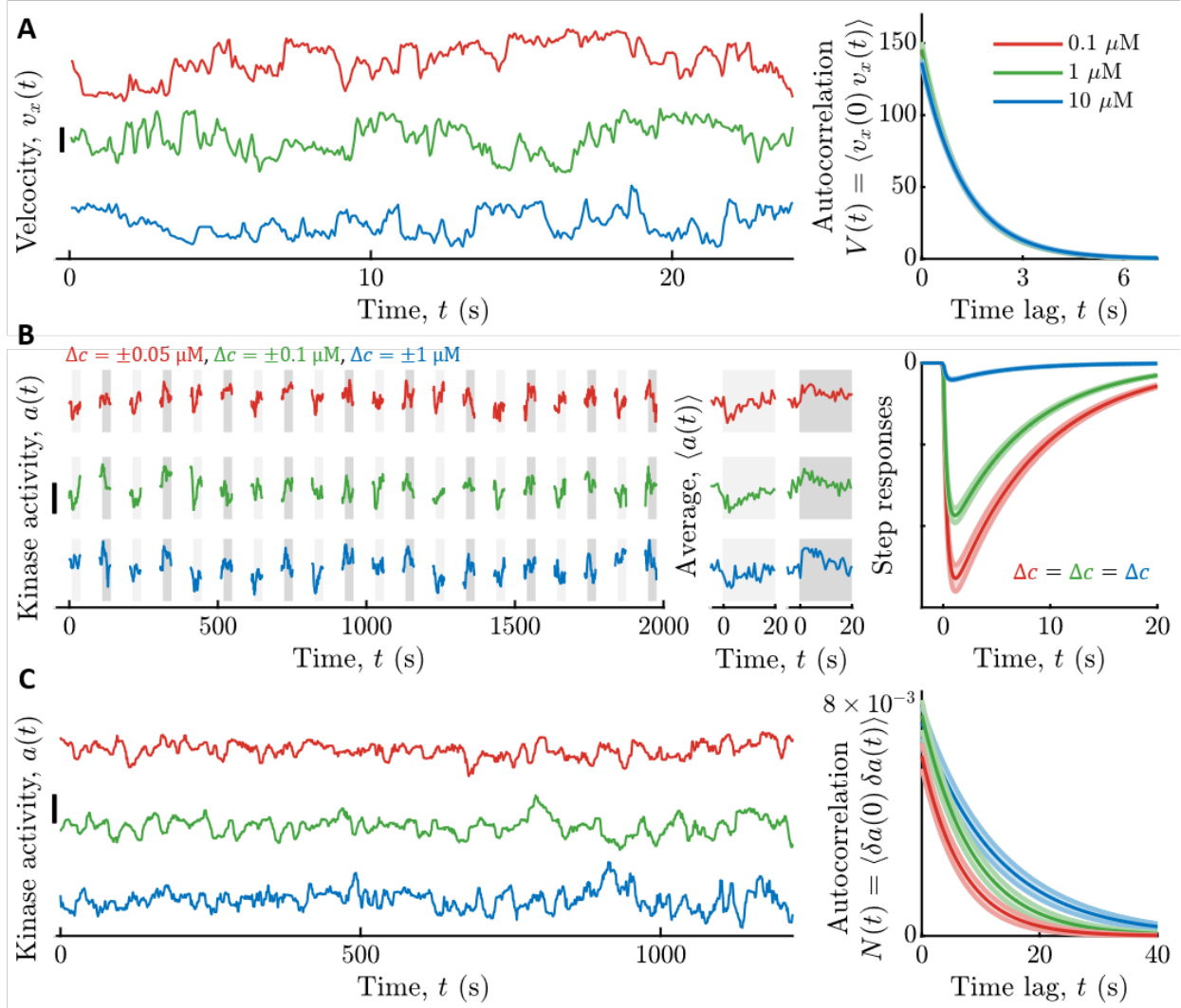


Figure 2: Measured signal statistics and kinase responses and fluctuations in different background ligand concentrations. **A)** Signal statistics. Left: Representative time series of up-gradient velocity v_x from three individual cells are shown, one in each background concentration c_0 . Scale bar is 20 $\mu\text{m/s}$. Cells were binned by the fraction of time they spend running, P_{run} , and the velocity autocorrelation function was computed by averaging over cells in the median bin ($P_{run} \approx 0.89$). The parameters of the velocity autocorrelation function were then fit with a decaying exponential $V(t) = \sigma_v^2 \exp\left(-\frac{t}{\tau_v}\right)$ to extract the velocity variance σ_v^2 and correlation time τ_v . Right: Model fits for velocity autocorrelation functions are shown for each c_0 . The curves are on top of each other. Units on the y-axis are $(\mu\text{m/s})^2$. Throughout, line colors indicate c_0 : Red: 0.1 μM Asp; Green: 1 μM Asp; Blue: 10 μM Asp, and shading is standard error of the mean (SEM). **B)** Linear responses. Left: Immobilized cells were continuously exposed with a constant background concentration c_0 of aspartate (Asp). The fraction of active kinases (kinase activity) was measured by FRET in blocks of 25 seconds, separated by 65 seconds without illumination. In each block, after 5 s, concentration was stepped up (light gray shading) or down (dark gray shading) around c_0 , then maintained for 20 s, and then returned to c_0 . Concentration step sizes Δc were different for each c_0 (shown above the panel). Shown are three representative cells, one from each c_0 . Scale bar is 0.3. Middle:

Average responses of the cells in the left panel to a step up (light gray) and step down (dark gray) of concentration. Single-cell responses were fit to the model in Eqn. 15 to extract single-cell parameters of the response function $K_r(t)$. Right: Using the median parameter values of the population, shown as model fits for kinase responses to a step increase in concentration of size Δc , for each background c_0 . The gain of the response G_r decreases with c_0 . **C)** Noise statistics. Left: Fluctuations in kinase activity were measured in constant background concentrations. Representative time series from three cells are shown, one in each background concentration. Scale bar height is 0.3. Parameters of the slow noise autocorrelation function (Eqn. 8), were fit to single-cell traces using Bayesian filtering (SI). Right: Estimated noise autocorrelation functions for the median cell are shown, for each background concentration c_0 . Units on the y-axis are kinase activity squared.

Comparing *E. coli* to the physical limit

We can now answer our central question: does the stochastic arrival of particles prevent *E. coli* from getting more information during chemotaxis? The remaining unknown needed to answer this is the diffusion-limited particle arrival rate constant, $k_D = 4 D l$. We take $l = 60$ nm (82) as a conservative lower estimate of the diameter of the receptor array and $D = 800$ $\mu\text{m}^2/\text{s}$ (83,84) as the ligand diffusivity. With these, we estimate that $k_D \approx 1.2 \times 10^5 \text{ s}^{-1} \mu\text{M}^{-1}$, indicating that about 10^5 independent molecules strike the cell's receptor array per second in a background of $c_0 = 1$ μM , which is comparable to previous estimates (2,8).

Both *E. coli*'s information rate, $\dot{I}_{s \rightarrow a}^*$, and the physical limit, $\dot{I}_{s \rightarrow r}^*$, are approximately proportional to the gradient steepness squared, g^2 in the limit of a shallow gradient (black lines in Fig. 3AB). Therefore, we quantify the information rates per g^2 , using the parameters measured in the previous section. In particular, we plot the full expressions for the information rates, which are given in the SI. In Fig. 3A, we plot these quantities as functions of background concentration c_0 , for varying values of the gradient steepness $g \in [0, 0.4]$ mm^{-1} , within which we observed linear dependence of chemotaxis drift speed on g (1). Doing so reveals that *E. coli* are surprisingly far from the physical limit: in shallow gradients, $\dot{I}_{s \rightarrow a}^*$ is at least two orders of magnitude below $\dot{I}_{s \rightarrow r}^*$ across all background concentrations.

To quantify the fidelity of *E. coli*'s chemical sensing relative to the physical limit, we computed the ratio of *E. coli*'s information rate relative to the physical limit, $\eta \equiv \frac{\dot{I}_{s \rightarrow a}^*}{\dot{I}_{s \rightarrow r}^*}$. We first focus on the limit of vanishingly small gradients, where η is independent of g , and we plot it in Fig. 3B (black) as a function of background concentration, c_0 . In low backgrounds, $c_0 \ll K_i$, the kinase signal-to-noise ratio, γ_a , scales as c_0^2 since *E. coli*'s gain G_r and noise in kinase activity are constant. Thus, *E. coli*'s information rate scales as $\dot{I}_{s \rightarrow a}^* \propto c_0^2$. Since the physical limit scales as $\dot{I}_{s \rightarrow r}^* \propto c_0$, we get $\eta \propto c_0$, which goes to zero with decreasing background concentration. In high backgrounds, $c_0 \gg K_i$, the kinase signal-to-noise ratio γ_a is approximately constant because the gain depends on background concentration as $G_r \propto 1/c_0$, which cancels the concentration-dependence of the molecular arrival rate, $r_0 \propto c_0$, and so $\dot{I}_{s \rightarrow a}^*$ is constant. As a result, we get $\eta \propto 1/c_0$, which again goes to zero with increasing concentration. These two regimes are separated by a peak at $c_0 = K_i$, where $\eta \approx 0.014 \pm 0.002$ at our closest measured data point (black in Fig. 3B). In this

background, the variance of filtered particle arrival noise is largest, but it is still much smaller than the variance of other kinase noise sources (see Figs. S1, S3).

For small but finite gradients, we find that η increases as the gradient g gets steeper, increasing to $\eta \approx 0.1$ when $g = 0.4 \text{ mm}^{-1}$. This smaller value of η does not imply that *E. coli* count every particle in steeper gradients. Instead, η increases with g because the information rate, $\dot{I}_{s \rightarrow r}^*$, saturates in steeper gradients (solid color lines decreasing with g in Fig. 3A). In a steep gradient, even a poor sensor can accurately infer the signal, $s(t)$, and increasing particle counts only provides marginal gains on the information rate. Mathematically, this can be seen through the weak dependence of $\dot{I}_{s \rightarrow r}^*$ on g outside of the small-signal regime (Fig. 3A). $\dot{I}_{s \rightarrow a}^*$, on the other hand, remains roughly proportional to g^2 to much steeper gradients. Thus, kinase activity is still in the small-signal regime in conditions where particle arrivals are not. In steeper gradients where signal can be reconstructed accurately, *E. coli* are able to get closer to the information bound even with a sensor that is far from counting every particle.

We support this further in Figs. 3CD. In Fig. 3C, we show the power spectrum of total noise in kinase activity (green line) compared to the power spectrum of filtered particle arrival noise (blue line). If *E. coli* were close to the particle-counting limit, nearly all noise in kinase activity would come from filtering particle arrivals; instead, kinase fluctuations are much larger over the range of frequencies observable in experiment (Fig. 3C, outside the pink region). We extrapolate to higher frequencies by conservatively assuming that the lines approach each other (black line), but it is possible that there are additional high frequency noise sources (putting the black line higher in shaded region of Fig 3C) or that the response function has a slower τ_1 than in our model (putting the blue line lower in pink shaded region of Fig 3C). The information rate is relatively insensitive to these choices (see SI Fig S3 for discussion). In Fig. 3D, we show the optimal reconstructions of $s(t)$ in Fig. 1, both from past particle arrivals $\{r\}$ and from past kinase activity $\{a\}$ using the parameter values determined from the experiments. The fidelity of the reconstruction from kinase activity is visibly worse than that from particle arrivals, consistent with the much lower information about the signal encoded in the kinase activity. Thus, *E. coli*'s information about signals during chemotaxis is not limited by the physical limit set by counting single particle arrivals.

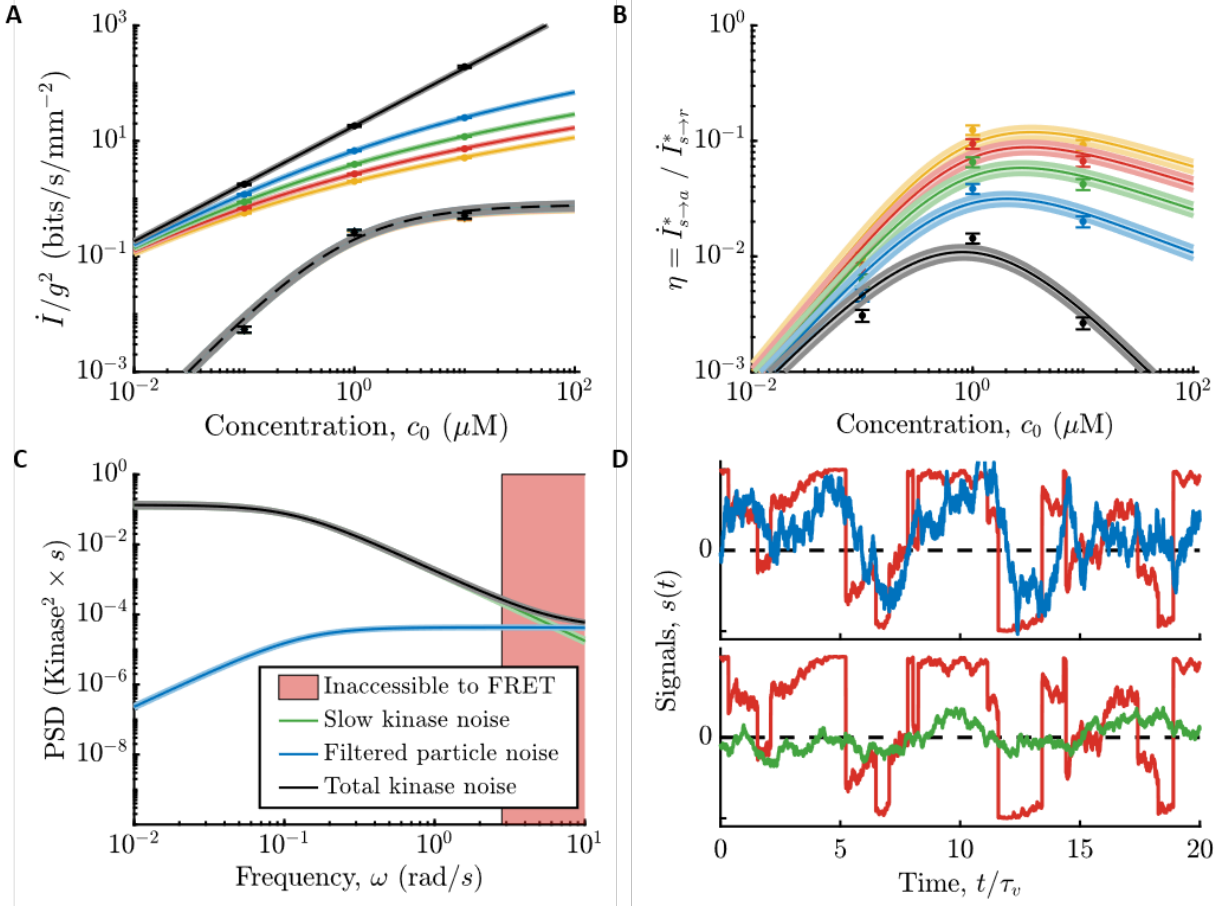


Figure 3: Comparing *E. coli*'s information rates to the particle counting limit. **A)** Information rates per gradient steepness squared, g^2 , in particle arrivals, $\dot{I}_{s \rightarrow r}^*$ (SI Eqn. 44; solid lines), and in kinase activity, $\dot{I}_{s \rightarrow a}^*$ (SI Eqn. 89; dashed lines use Eqn. 16 and parameters measured in $c_0 = 1 \mu\text{M}$) for gradients of varying steepness, $g \in \{0^+, 0.1, 0.2, 0.3, 0.4\} \text{ mm}^{-1}$ in black, blue, green, red, yellow, where black is the small gradient limit, $g \rightarrow 0$. Dots are experimental measurements. Error bars and shading throughout are SEM. We find that *E. coli* far from the physical limit set by particle arrivals when signals are weak and sensor quality matters. In particular, the fundamental limit $\dot{I}_{s \rightarrow r}^*$ scales slower than g^2 , even for moderate g , indicating that it is out of the small-signal regime. Information in kinase activity $\dot{I}_{s \rightarrow a}^*$, on the other hand, is roughly proportional to g^2 (the lines are on top of each other), indicating that *E. coli* are still in the small-signal regime. **B)** $\eta = \dot{I}_{s \rightarrow a}^* / \dot{I}_{s \rightarrow r}^*$ versus c_0 . Colors and markers are same as in (A). In steeper gradients, the quality of *E. coli*'s chemosensory apparatus matters less for getting close to the limit. **C)** Fit models for the noise power spectra in background concentration $c_0 = 1 \mu\text{M}$. Green: fit to measured slow noise in kinase activity. Blue: particle arrival noise filtered through kinase response kernel. Black: Sum of green and blue, used as a conservative estimate of information in kinase activity. Red shading: experimentally-inaccessible region using CheY-CheZ FRET. See also SI Fig. S3 and the SI section "Modeling kinase activity" for discussion about noise in the red region. If *E. coli* were close to the physical limit, the black line would be close to the blue line at all frequencies. Instead, excess slow noise in kinase activity dominates over the entire range of observable frequencies. **D)** *E. coli*'s low information rates relative to the physical limit correspond to poor estimates of the signal $s(t)$. Red: true signal from Fig. 1 with $c_0 = 1 \mu\text{M}$ and $g = 0.3 \text{ mm}^{-1}$. Top, blue: reconstructed signal from particle arrival rate r in Fig. 1, using the optimal causal kernel (SI Eqn. 57).

Bottom, green: reconstructed signal from kinase activity a in Fig. 1, using the optimal causal kernel (SI Eqn. 95).

Discussion

Here, we studied how the physics of chemosensing (2) limits *E. coli*'s ability to encode information about signals relevant for chemotaxis. We derived a physical limit on information about the current time derivative of concentration, which we previously showed cells need for chemotaxis (1), by considering an ideal sensor able to register the arrival of every particle at its surface. We then measured the rate at which *E. coli* encode this information into the activity of their receptor-associated kinases through a series of single-cell measurements in multiple background concentrations of attractant. We found that *E. coli* are far from the physical limit of an idealized sensor, getting only a few percent of the information available in ligand particle arrivals in shallow gradients. Thus, the fidelity of *E. coli*'s chemosensing, and hence their chemotaxis performance, is not limited by the physics of molecule counting.

Previous work anticipated that *E. coli* would be much closer to the particle counting limit. Berg and Purcell argued that, in *E. coli* and *Salmonella typhimurium* chemotaxis, the change in concentration over a single run in a typical gradient could be estimated by an ideal agent with uncertainty smaller than the mean (2). From this, they concluded that the bacterial chemotaxis machinery is nearly optimal. However, their calculation does not imply that bacteria actually achieve that level of accuracy. Ref. (8) fit agent-based simulations to experimental measurements of *Vibrio ordalii* climbing dynamic chemical gradients and argued that this bacterium is within a factor of ~ 6 of the particle counting limit. However, this analysis assumed that cells infer $s(t)$ in short, independent time windows of duration $T = 0.1$ s. Instead, real cells continuously monitor new particle arrivals and forget old ones, allowing them to average out molecule counting noise for integration times up to the signal correlation time τ_v . This increases the theoretical maximum precision in the analysis of Ref. (8), and thus *V. ordalii*'s distance from the limit, by a factor of $(\tau_v/T)^3 = \left(\frac{0.45 \text{ s}}{0.1 \text{ s}}\right)^3 \sim 90$, due to the T^3 in the uncertainty about signal (35). We believe this explains the discrepancy between our findings. It also suggests that similar constraints might limit the sensing fidelity of *E. coli* and other bacterial species.

We discovered a new relationship between two previously-disconnected information quantities: the transfer entropy rate (40) and the predictive information (42). While past work has argued that signaling networks should carry predictive information (12,13,42,44,45), here we identify a specific behavior where performance depends quantitatively on a predictive information rate. This new predictive information rate allows us to distinguish two possible sources of inefficiency that we could not separate in our previous study (1). First, kinases could encode information about past signals s , which do not contribute to gradient climbing; and second, relevant information could be lost in communication with the motors. Using $\dot{I}_{s \rightarrow a}^*$ derived here, which isolates information about the present signal, we estimate that about 90% or more of the cell's information rate to kinase activity is relevant to chemotaxis, depending on c_0 (see SI), implying that the remaining losses are in communication with the motor.

Our analysis has implications for how we think about intermediary variables in signal transduction pathways. While behavioral decisions often require information about a current (or possibly future)

external signal, intermediate variables do not need to represent these in their current value. For example, the entire past trajectory of kinase activity, $\{a\}$, contains more information than its current value, a , about the current signal, s . This information can be extracted by downstream processing, all the way down to the motors (see SI section “Optimal kernel for estimating signal from kinase activity”). The information available to downstream processing is quantified by the predictive information rate, and critically, this quantity is agnostic to that processing. Here we took advantage of this property to measure the fidelity of the kinases without assuming their activity is an instantaneous, noisy readout of signal.

Why are *E. coli* so far from the particle counting limit? It may be that design constraints prevent them from reaching this limit. *E. coli* must be able to perform chemotaxis over many orders of magnitude in background concentration, which might impose trade-offs that prevent the system from achieving optimality. Fold-change detection enables this (79–81), but also causes *E. coli*'s gain, G_r , to decrease with increasing concentration (Methods). Thus, just to keep η from decreasing with c_0 , *E. coli* would need to have kinase noise variance that decreases with concentration like $1/c_0$. Instead, we find that it is roughly constant. Suppressing fluctuations or amplifying signals generally requires spending energy or resources (10–16,86,87), and those costs might not be worth the fitness benefit in this case. The mechanism of amplification is not well understood, but recent work has argued that it consumes energy (87–89). Thus, energetic and mechanical constraints might provide currently-unknown bounds on *E. coli*'s sensory fidelity.

Surely, *E. coli* have evolved under selection pressures other than climbing shallow gradients of aspartate. *E. coli* need to sense multiple ligands, such as amino acids, sugars, and peptides (62,90), some of which require different receptor types. But the presence of multiple receptor types in the receptor array reduces the cooperativity to any one ligand (74), while likely still contributing to signaling noise. *E. coli* may be under selection pressure not only to climb gradients but also to stay close to concentration peaks (18,19,92,93). Furthermore, we do not know the typical gradient steepness they have been selected to climb effectively. In an infinitely shallow gradient, we showed that an ideal sensor would allow a bacteria to climb gradients at least 10 times faster than typical *E. coli* (due to $I_{s \rightarrow a}^*/I_{s \rightarrow r}^* \approx 0.01$ and $v_d \propto (I_{s \rightarrow a}^*)^{1/2}$ (1)). However, in steeper gradients, where even a poor sensor can adequately measure direction, these gains would be far smaller. For example, in a relatively steep 500-micron gradient and background of 1 μM of attractant, we estimate that a typical cell would get $\sim 37\%$ of the relevant information available to an ideal sensor, and could climb $\sim 60\%$ as fast. It may be that the typical gradients that have driven the evolution of *E. coli*'s sensory apparatus are sufficiently steep as to obviate the need for an ideal single-molecule sensor. In the laboratory, the amino acid gradients *E. coli* perceive when migrating collectively are typically of order ~ 1 mm (93), and theory predicts that they can be steeper in semisolid agar (94,95) in which our laboratory strain of *E. coli* was selected for chemotaxis (96–98).

Existing findings give qualitative support for the idea that *E. coli* are not at the fundamental limit. Berg and Purcell's original paper argued that by evenly-distributing small, sparse receptors on its surface, a cell can make its ligand sensor nearly as effective as if its entire surface were covered with receptors (2). Thus, a chemosensor limited primarily by the noise of single particle arrivals would want to spread a limited receptor budget evenly over the cell surface to maximize the rate at which unique particles are counted. Instead, bacterial chemoreceptors are clustered in densely-packed arrays. This dense packing, which appears to be universal across species (99), might be necessary for bacteria to integrate and amplify signal that must be communicated to the motor to make all-or-none behavioral decisions.

Future experiments could probe whether hard constraints prevent *E. coli* from being close to the physical limit, or if tradeoffs would allow a cell to do better, perhaps at the cost of increased energy expenditure. This could be done by measuring information rates in single cells, where cell-to-cell variability (63,66–68,70,72,78,101,102) might enable some cells to be closer to the physical limit by chance.

While *E. coli* do not achieve the particle counting bound, their sensory capabilities are impressive. In the log-sensing regime they acquire and communicate information to the motor at a rate equivalent to an ideal sensor able to count several thousand particles every second. While current modeling efforts in chemosensing have mostly focused on quantitatively describing experimental observations, this work opens up new possibilities for a reverse engineering perspective. Our work highlights the need to understand how these systems achieve the signal processing, bandwidth, and fidelity needed for behavior, and how physical, geometric, and energetic constraints have shaped their evolution.

Methods

Modeling of average kinase responses to past signal versus past particle arrival rate

In our previous work (1), we modeled responses of kinase activity to past signals s instead of past particle arrival rate r . These two descriptions are equivalent in the regime of shallow gradients. We show this below by starting from average responses of kinase activity to particle arrival rate:

$$\langle a(t) \rangle = a_0 - \int_{-\infty}^t K_r(t-t') (\langle r(t') \rangle - r_0) dt', \quad (10)$$

where angled brackets indicate averaging over repeated presentation of the same signal trajectory $\{s\}$, and thus they average out particle noise and kinase noise. From here, we will derive a response kernel to past signals that gives identical kinase responses.

First, we note that:

$$\langle r(t) \rangle - r_0 = k_D (c(t) - c_0) = r_0 \int_{-\infty}^t s(t') dt', \quad (11)$$

where we used $s(t) \approx \frac{1}{c_0} \frac{dc}{dt}$ in shallow gradients.

It is convenient to transform the expressions above to Fourier space, where $\delta a(\omega) = F[\langle a(t) \rangle - a_0]$, $\delta r(\omega) = F[\langle r(t) \rangle - r_0]$, $K_r(\omega) = F[K_r(t)]$, and $F[f(t)] = \int_{-\infty}^{\infty} f(t) e^{i\omega t} dt$ is the Fourier transform. Then we have

$$\delta a(\omega) = -K_r(\omega) \delta r(\omega), \quad (12)$$

$$\delta r(\omega) = r_0 \frac{s(\omega)}{-i\omega}. \quad (13)$$

With this, we get:

$$\delta a(\omega) = -K_r(\omega) r_0 \frac{s(\omega)}{-i\omega} = -K(\omega) s(\omega) \quad (14)$$

where $K(\omega) = r_0 \frac{K_r(\omega)}{-i\omega}$ is the Fourier transform of the linear response function to signals. Thus, we can either write down average kinase responses to particle arrival rate $r(t)$, with linear response function $K_r(t)$, or responses to signals $s(t)$, with linear response function $K(t)$ (1):

$$K(t) = r_0 \int_0^t K_r(t') dt' = G \exp\left(-\frac{t}{\tau_2}\right) \left(1 - \exp\left(-\frac{t}{\tau_1}\right)\right). \quad (15)$$

where we have defined the MWC model gain $G = r_0 G_r$ (23,76). Thus:

$$G_r = \frac{1}{r_0} G \approx \frac{1}{k_D c_0 + K_i} \frac{G_\infty}{r_0}. \quad (16)$$

We can use the response function to particle arrivals, $K_r(t)$, to compute the power spectrum of particle counting noise filtered through the kinase response kernel, $K_r(t)$, but expressed it in terms of the response kernel $K(t)$ to signals s . Since we model particle arrival noise as shot noise, its power spectrum is constant and equal to r_0 . Filtering this noise through the response kernel $K_r(\omega)$ gives:

$$N_r(\omega) = r_0 |K_r(\omega)|^2 = r_0 \left| \frac{-i\omega}{r_0} K(\omega) \right|^2 = \frac{1}{r_0} \omega^2 |K(\omega)|^2. \quad (17)$$

Simulation details in Figure 1

Simulation time step was $dt = 3 \times 10^{-3} \tau_v$. Signal $s(t)$ was simulated in 2D by randomly sampling the times of instantaneous tumbles, plus rotational diffusion during runs, which was implemented using the Euler-Maruyama method. Average particle arrival rate $\langle r(t) \rangle$ was computed from the signal, and then Gaussian noise of variance $\sqrt{r_0 dt}$ was added to mimic shot noise. Kinase activity $a(t)$ was simulated using the model in the main text (Eqn. 6), with biologically reasonable parameters (see Fig. 2).

Strains and plasmids

All strains and plasmids used are the same as in our recent work (1). The strain used for the FRET experiments is a derivative of *E. coli* K-12 strain RP437 (HCB33), a gift of T. Shimizu, and described in detail elsewhere (59,70). The FRET acceptor-donor pair (CheY-mRFP and CheZ-mYFP) is expressed in tandem from plasmid pSJAB106 (59) under an isopropyl β -D-thiogalactopyranoside (IPTG)-inducible promoter. The glass-adhesive mutant of FliC (FliC*) was expressed from a sodium salicylate (NaSal)-inducible pZR1 plasmid (59). The plasmids are transformed in VS115, a *cheY cheZ fliC* mutant of RP437 (59) (gift of V. Sourjik). RP437, the direct parent of the FRET strain and also a gift from T. Shimizu, was used to measure swimming statistics parameters. All strains are available from the authors upon request.

Cell preparation

Single-cell FRET microscopy and cell culture was carried out essentially as described previously (1,59,70,72). Cells were picked from a frozen stock at -80°C and inoculated in 2 mL of Tryptone Broth (TB; 1% bacto tryptone, 0.5 % NaCl) and grown overnight to saturation at 30°C and shaken at 250 RPM. Cells

from a saturated overnight culture were diluted 100X in 10 mL TB and grown to OD600 0.45-0.47 in the presence of 100 µg/ml ampicillin, 34 µg/ml chloramphenicol, 50 µM IPTG and 3 µM NaSal, at 33.5°C and 250 RPM shaking. Cells were collected by centrifugation (5 min at 5000 rpm, or 4080 RCF) and washed twice with motility buffer (10 mM KPO₄, 0.1 mM EDTA, 1 µM methionine, 10 mM lactic acid, pH 7), and then were resuspended in 2 mL motility buffer, plus the final concentration of Asp. Cells were left at 22°C for 90 minutes before loading into the microfluidic device. All experiments, FRET and swimming, were performed at 22-23°C.

For swimming experiments, cells were prepared similarly. Saturated overnight cultures were diluted 100X in 5 mL of TB. After growing to OD600 0.45-0.47, 1 mL of cell suspension was washed twice in motility buffer with 0.05% w/v of polyvinylpyrrolidone (MW 40 kDa) (PVP-40). Washes were done by centrifuging the suspension in an Eppendorf tube at 1700 RCF (4000 RPM in this centrifuge) for 3 minutes. After the last wash, cells were resuspended with varying background concentrations of Asp.

Microfluidic device fabrication and loading for FRET measurements

Microfluidic devices for the FRET experiments (70–72) were constructed from polydimethylsiloxane (PDMS) on 24 x 60 mm cover glasses (#1.5) following standard soft lithography protocols (102), exactly as done before (1).

Sample preparation in the microfluidic device was conducted as follows. Five inlets of the device were connected to reservoirs (Liquid chromatography columns, C3669; Sigma Aldrich) filled with motility buffer containing various concentrations of Asp through polyethylene tubing (Polythene Tubing, 0.58 mm id, 0.96 mm od; BD Intermedic) (see SI of (1)). The tubing was connected to the PDMS device through stainless steel pins that were directly plugged into the inlets or outlet of the device (New England Tubing). Cells washed and suspended in motility buffer were loaded into the device from the outlet and allowed to attach to the cover glass surface via their sticky flagella by reducing the flow speed inside the chamber. The pressure applied to the inlet solution reservoirs was controlled by computer-controlled solenoid valves (MH1; Festo), which rapidly switched between atmospheric pressure and higher pressure (1.0 kPa) using a source of pressurized air. Only one experiment was conducted per device. *E. coli* consume Asp, so all experiments below were performed with a low dilution of cells to minimize this effect. The continuous flow of fresh media also helped ensure that consumption of Asp minimally affected the signal cells experienced.

Single-cell FRET imaging system

FRET imaging in the microfluidic device was performed using the setup as before (1), on an inverted microscope (Eclipse Ti-E; Nikon) equipped with an oil-immersion objective lens (CFI Apo TIRF 60X Oil; Nikon). YFP was illuminated by an LED illumination system (SOLA SE, Lumencor) through an excitation bandpass filter (FF01-500/24-25; Semrock) and a dichroic mirror (FF520-Di02-25x36; Semrock). The fluorescence emission was led into an emission image splitter (OptoSplit II; Cairn) and further split into donor and acceptor channels by a second dichroic mirror (FF580-FDi01-25x36; Semrock). The emission was then collected through emission bandpass filters (F01-542/27-25F and FF02-641/75; Semrock; Semrock) by a sCMOS camera (ORCA-Flash4.0 V2; Hamamatsu). RFP was illuminated in the same way as

YFP except that an excitation bandpass filter (FF01-575/05-25; Semrock) and a dichroic mirror (FF593-Di03-25x36; Semrock) were used. An additional excitation filter (59026x; Chroma) was used in front of the excitation filters. To synchronize image acquisition and the delivery of stimulus solutions, a custom-made MATLAB program controlled both the imaging system (through the API provided by Micro-Manager (103)) and the states of the solenoid valves.

Computing FRET signal and kinase activity

FRET signals were extracted from raw images using the E-FRET method (104), which corrects for different rates of photobleaching between donor and acceptor molecules. In this method, YFP (the donor) is illuminated and YFP emission images (I_{DD}) and RFP (the acceptor) emission images (I_{DA}) are captured. Periodically, RFP is illuminated and RFP emission images are captured (I_{AA}). From these, photobleach-corrected FRET signal is computed as before (1), which is related to kinase activity $\alpha(t)$ by an affine transform when CheY and CheZ are overexpressed (1,73). All parameters associated with the imaging system were measured previously (1).

In each experiment, we first delivered a short saturating stimulus (1 mM MeAsp plus 100 μ M serine (74)) to determine the FRET signal at minimum kinase activity, followed by motility buffer with Asp at background concentration c_0 . Before the saturating stimulus was delivered, the donor was excited every 0.5 seconds to measure I_{DD} and I_{DA} (see SI of (1)) for 5 seconds. Then the stimulus was delivered for 10 seconds, and the donor was excited every 0.5 seconds during this time. Before and after the donor excitations, the acceptor was excited three times in 0.5-second intervals to measure I_{AA} (see SI of (1)). After the stimulus was removed, the acceptor was excited three more times at 0.5-second intervals. Imaging was then stopped and cells were allowed to adapt to the background for 120 seconds.

Stimulus protocols for measuring kinase linear response functions and fluctuations are described below.

At the end of each experiment, we delivered a long saturating stimulus (1 mM MeAsp plus 100 μ M serine) for 180 seconds to allow the cells to adapt. Then we removed the stimulus back to the background concentration, eliciting a strong response from the cells, from which we determined the FRET signal at maximum kinase activity. The donor was excited for 5 seconds before the saturating stimulus and 10 seconds after it, every 0.5 seconds. Before and after these donor excitations, the acceptor was excited three times in 0.5-second intervals. The cells were exposed to the saturating stimulus for 180 seconds. The donor was excited every 0.5 seconds for 5 seconds before cells were exposed to motility buffer with Asp at background concentration c_0 , followed by 10 seconds of additional donor excitations. Before and after the donor excitations, the acceptor was again excited three times in 0.5-second intervals.

FRET signals were extracted as before (1). The FRET signal at minimum kinase activity, $FRET_{min}$, was computed from the average FRET signal during the first saturating stimulus. The FRET signal at maximum kinase activity, $FRET_{max}$, was computed from the average FRET signal during the first quarter (2.5 seconds) of the removal stimulus at the end of the experiment. Kinase activity was then computed from corrected FRET signal: $\alpha(t) = \frac{FRET(t) - FRET_{min}}{FRET_{max} - FRET_{min}}$.

Kinase linear response functions

Experiments were performed in Asp background concentrations c_0 of 0.1, 1, and 10 μM . Measurements were made in single cells, and at least three replicates were performed per background. FRET level at minimum kinase activity was measured at the beginning of each experiment, as described above. After this, a series of stimuli were delivered to the cells in the microfluidic device. Cells were only illuminated and imaged when stimulated in order to limit photobleaching. Before each stimulus, cells were imaged for 7.5 seconds in the background concentration c_0 . Then, the concentration of Asp was shifted up to $c_+ > c_0$ for 30 seconds and imaging continued. Donor excitation interval was 0.75 seconds and acceptor excitations were done before and after the set of donor excitations. After this, imaging was stopped and the Asp concentration returned to c_0 for 65 seconds to allow cells to adapt. Then, the same process was repeated, but this time shifting Asp concentration down to $c_- < c_0$. Alternating up and down stimuli were repeated 10 times each. c_+ and c_- varied with each experiment and each background c_0 . Finally, FRET level at maximum kinase activity was measured at the end of each experiment, as described above. The whole imaging protocol lasted <2200 seconds. In total, cells spent <60 minutes in the device, from loading to the end of imaging.

These data were analyzed as before (1) to extract linear response parameters for each cell. In brief, the responses of a cell to all steps up or steps down in concentration were averaged and the standard error of the response at each time point computed. Model parameters were extracted by maximizing the posterior probability of parameters given data, assuming a Gaussian likelihood function and log-uniform priors for the parameters. The uncertainties of single-cell parameter estimates were generated by MCMC sampling the posterior distribution. Finally, the population-median parameters were computed from all cells in experiments in a given background c_0 . Uncertainty $\sigma_{\theta_i}^2$ of the population-median value of parameter θ_i , with $\theta = (G, \tau_1, \tau_2)$, was computed using:

$$\sigma_{\theta_i}^2 = \frac{1}{N} \left(1.4826 \text{ mad}(\{\theta_i^{MAP}\}) \right)^2 + \frac{1}{N^2} \sum_k (\sigma_{\theta_i}^2)_k. \quad (18)$$

This expression accounts both for cell-to-cell variations (first term) and uncertainties in the single-cell estimates (second term). N is the number of cells. $1.4826 \text{ mad}(\)$ is an outlier-robust uncertainty estimate that coincides with the standard deviation when the samples are Gaussian-distributed, and $\text{mad}(\)$ is the median absolute deviation, used previously (1). $\{\theta_i^{MAP}\}$ are the single-cell maximum *a-posteriori* (MAP) estimates of parameter θ_i . $(\sigma_{\theta_i}^2)_k$ is the uncertainty of θ_i^{MAP} in cell k , which was computed using

$$(\sigma_{\theta_i})_k = 1.4826 \text{ mad}(\{\hat{\theta}_i\}_k) \quad (19)$$

where $\{\hat{\theta}_i\}_k$ are the samples from the k th cell's posterior via Markov Chain Monte Carlo (MCMC).

MWC kinase gain

The estimated gain parameter G depended strongly on c_0 , consistent with expectations from previous work modeling kinase activity using the MWC model (e.g. (76)). In the MWC model, kinase-receptor complexes can be in active or inactive states. The dissociation constants for the attractant in each state, K_i and K_a , are different, with $K_i \ll K_a$, which causes attractant concentration to influence the fraction of

kinases in the active state. When the background concentration $c_0 \ll K_a$, the gain of the kinase response to changes in log-concentration of attractant can be written:

$$G(c_0) = G_\infty \frac{c_0}{c_0 + K_i},$$

where G_∞ is the “log-sensing” gain (when $c_0 \gg K_i$). Parameters G_∞ and K_i were estimated by fitting the estimates of G versus c_0 . The fit was done by minimizing the sum of squared errors between the logarithms of G and G_{MWC} . The estimated values of G vary by about an order of magnitude, and taking the logarithms ensured that the smallest value of G had similar weight as largest value in the objective function.

Statistics of noise in kinase activity

Fluctuations in kinase activity were measured in the same Asp background concentrations c_0 as above, as well as $c_0 = 0 \mu\text{M}$. At least three replicate experiments were performed per background. FRET level at minimum kinase activity was measured at the beginning of each experiment, as described above. After these measurements, imaging was then stopped and cells were allowed to adapt to the background for 120 seconds. After this, cells were imaged for about 1200 seconds. Throughout, donor excitations were done every 1.0 second, except when it was interrupted by acceptor excitations, which were conducted every 100 donor excitations (see SI of (1)). Finally the FRET level at maximum kinase activity was measured at the end of each experiment, as described above. The whole imaging protocol lasted <1400 seconds. In total, cells spent about < 60 minutes in the device, from loading to the end of imaging.

These data were analyzed as before (1). Bayesian filtering methods (82) were used to compute the likelihood of the parameters given the data, and the prior distribution was taken to be uniform in log. Single-cell estimates and uncertainties of the noise parameters were extracted from the posterior distribution as described above. In each background c_0 , the population median parameter values were computed, and their uncertainties were computed as described above, with $\theta = (D_n, \tau_n)$.

Swimming velocity statistics

Cells were prepared and imaged as before (1). After the second wash step of the Cell preparation section above, cells were centrifuged again and resuspended in motility buffer containing a background concentration of Asp c_0 . The values of c_0 used here were the same as in the FRET experiments, including $c_0 = 0 \mu\text{M}$. Then, the cell suspension was diluted to an OD600 of 0.00025. This low dilution of cells both enables tracking and minimizes the effect of cells consuming Asp. The cell suspension was then loaded into μ -Slide Chemotaxis devices (ibidi; Martinsried, Germany). Swimming cells were tracked in one of the large reservoirs. 1000-s movies of swimming cells were recorded on a Nikon Ti-E Inverted Microscope using a CFI Plan Fluor 4X objective (NA 0.13). Images were captured using a sCMOS camera (ORCA-Flash4.0 V2; Hamamatsu). Four biological replicates were performed for each background c_0 .

Cell detection and tracking were carried out using the same custom MATLAB as we used previously (1), with the same analysis parameters (see SI of that paper for details). Tumble detection was also carried out identically as before (1). There was no minimum trajectory duration, but cells were kept only if at least

two tumbles were detected in their trajectory. For each cell, we computed the fraction of time spent in the “run” state P_{run} . Then we constructed the distribution of P_{run} , correcting for biases caused by the different diffusivities of cells with different P_{run} (1). As before (1), we then computed the correlation function of velocity along one spatial dimension for each cell, $V_i(t) = \langle v_x(t')v_x(t'+t) \rangle_{t'}$ among cells with P_{run} within ± 0.01 of the population-median value. Finally, we computed a weighted average of the correlation functions over all cells in the population-median bin of P_{run} , where trajectories were weighted by their duration, giving $V(t)$. In each background c_0 , for the median bin of P_{run} , the average trajectory duration was ~ 7.6 seconds, and the total trajectory time was $\geq 2.7 \times 10^4$ seconds.

These correlation functions $V(t)$ in each background c_0 and each experiment were fit to decaying exponentials $\sigma_v^2 \exp(-|t|/\tau_v)$, and the parameters and their uncertainties were extracted in two steps. First, we determined the MAP estimates of the parameters. An initial estimate of the parameters were estimated using the MATLAB *fit* function to fit exponentials to the $V(t)$ in the time range $t \in [2 \Delta t, 10 \text{ s}]$, with $\Delta t = 50$ ms. The estimated τ_v was used to get the uncertainty of $V(t)$ in each experiment, as done before (1). Assuming a Gaussian likelihood function and parameters distributed uniformly in logarithm, the posterior distribution of parameter was constructed. In each experiment, MAP estimates of the parameters were extracted as done for the kinase parameters, and parameter uncertainties were computed from MCMC samples of the posterior distribution as above. Finally, we computed the average parameters σ_v^2 and τ_v over experimental replicates, as well as their standard errors over replicates.

Additional error analysis

Once the variance of the population-median value of parameter i was computed, $\sigma_{\theta_i}^2$, we propagated the uncertainty to functions of those parameters. For some function of the parameters, $f(\theta)$, we computed the variance of $f(\theta)$, σ_f^2 , as:

$$\begin{aligned} \sigma_f^2 &= \sum_i \left(\frac{\partial f}{\partial \theta_i} \right)^2 \sigma_{\theta_i}^2 \\ &= f^2 \sum_i \left(\frac{\partial \log f}{\partial \theta_i} \right)^2 \sigma_{\theta_i}^2. \end{aligned} \quad (20)$$

The equations above neglect correlations in the uncertainties between pairs of parameters. This was used to compute the uncertainties of $\dot{I}_{S \rightarrow r}^*$, $\dot{I}_{S \rightarrow a}^*$, and η . The same formula was used to compute uncertainties of functions of time by applying the formula above pointwise at each time delay t and neglecting correlations in uncertainties between time points.

Acknowledgments: We thank ... This work was supported by the Alfred P. Sloan Foundation under grant G-2023-19668 (HM, TE, BB); by NIH awards R01GM106189 (TE), R01GM138533 (TE), and R35GM138341 (BM); by Simons Investigator Award 624156 (BM); and by the JST PRESTO grant JPMJPR21E4 (KK); by the NSTC grant 112-2112-M-001-080-MY3. HM was supported by the Flatiron Institute, which is a division of the Simons Foundation. KK was also supported by the Institute of Molecular Biology, Academia Sinica.

Contributions: BM and HM conceived the project. KK, HM, TE, and BM designed the experiments. KK, JO, RK, and HM performed the experiments. HM and KK analyzed the data. HM and BM derived the theoretical results. HM wrote the first draft of the manuscript. HM, BM, KK, and TE edited the manuscript.

Competing interests: The authors declare no competing interests.

Data availability: Source data for the main text figures are provided online with the manuscript. Source data for the Supplementary Figures are contained in a Supplementary Data file.

Code availability: Code to reproduce the main text figures are available with the source data. All algorithms used are described in detail in the Supplementary Information.

References

1. Mattingly HH, Kamino K, Machta BB, Emonet T. Escherichia coli chemotaxis is information limited. *Nat Phys*. 2021 Dec;17(12):1426–31.
2. Berg HC, Purcell EM. Physics of chemoreception. *Biophysical Journal*. 1977 Nov 1;20(2):193–219.
3. Osborne LC, Lisberger SG, Bialek W. A sensory source for motor variation. *Nature*. 2005 Sep;437(7057):412–6.
4. Hecht S, Shlaer S, Pirenne MH. ENERGY, QUANTA, AND VISION. *Journal of General Physiology*. 1942 Jul 20;25(6):819–40.
5. Barlow HB. The Size of Ommatidia in Apposition Eyes. *Journal of Experimental Biology*. 1952 Dec 1;29(4):667–74.
6. Rieke F, Baylor DA. Single-photon detection by rod cells of the retina. *Rev Mod Phys*. 1998 Jul 1;70(3):1027–36.
7. Bialek W. *Biophysics: Searching for Principles* [Internet]. Princeton University Press; 2012 [cited 2020 Jun 18]. Available from: <https://press.princeton.edu/books/hardcover/9780691138916/biophysics>
8. Brumley DR, Carrara F, Hein AM, Yawata Y, Levin SA, Stocker R. Bacteria push the limits of chemotactic precision to navigate dynamic chemical gradients. *PNAS*. 2019 May 28;116(22):10792–7.
9. Sinha SR, Bialek W, van Steveninck RR de R. Optimal Local Estimates of Visual Motion in a Natural Environment. *Phys Rev Lett*. 2021 Jan 4;126(1):018101.
10. Govern CC, Wolde PR ten. Optimal resource allocation in cellular sensing systems. *PNAS*. 2014 Dec 9;111(49):17486–91.
11. Malaguti G, ten Wolde PR. Theory for the optimal detection of time-varying signals in cellular sensing systems. Goldstein RE, Weigel D, editors. *eLife*. 2021 Feb 17;10:e62574.
12. Tjalma AJ, Galstyan V, Goedhart J, Slim L, Becker NB, ten Wolde PR. Trade-offs between cost and information in cellular prediction. *Proceedings of the National Academy of Sciences*. 2023 Oct 10;120(41):e2303078120.
13. Tjalma AJ, Wolde PR ten. Predicting concentration changes via discrete sampling [Internet]. *arXiv*; 2024 [cited 2024 Feb 15]. Available from: <http://arxiv.org/abs/2402.05825>
14. Lan G, Sartori P, Neumann S, Sourjik V, Tu Y. The energy–speed–accuracy trade-off in sensory adaptation. *Nature Physics*. 2012 May;8(5):422–8.
15. Cao Y, Wang H, Ouyang Q, Tu Y. The free-energy cost of accurate biochemical oscillations. *Nature Phys*. 2015 Sep;11(9):772–8.

16. Zhang D, Cao Y, Ouyang Q, Tu Y. The energy cost and optimal design for synchronization of coupled molecular oscillators. *Nat Phys*. 2020 Jan;16(1):95–100.
17. Bryant SJ, Machta BB. Physical Constraints in Intracellular Signaling: The Cost of Sending a Bit. *Phys Rev Lett*. 2023 Aug 7;131(6):068401.
18. Clark DA, Grant LC. The bacterial chemotactic response reflects a compromise between transient and steady-state behavior. *PNAS*. 2005 Jun 28;102(26):9150–5.
19. Celani A, Vergassola M. Bacterial strategies for chemotaxis response. *PNAS*. 2010 Jan 26;107(4):1391–6.
20. Cremer J, Honda T, Tang Y, Wong-Ng J, Vergassola M, Hwa T. Chemotaxis as a navigation strategy to boost range expansion. *Nature*. 2019 Nov;575(7784):658–63.
21. Ni B, Colin R, Link H, Endres RG, Sourjik V. Growth-rate dependent resource investment in bacterial motile behavior quantitatively follows potential benefit of chemotaxis. *PNAS*. 2020 Jan 7;117(1):595–601.
22. Shimizu TS, Tu Y, Berg HC. A modular gradient-sensing network for chemotaxis in *Escherichia coli* revealed by responses to time-varying stimuli. *Molecular Systems Biology*. 2010 Jan 1;6(1):382.
23. Tu Y. Quantitative Modeling of Bacterial Chemotaxis: Signal Amplification and Accurate Adaptation. *Annual Review of Biophysics*. 2013;42(1):337–59.
24. Parkinson JS, Hazelbauer GL, Falke JJ. Signaling and sensory adaptation in *Escherichia coli* chemoreceptors: 2015 update. *Trends in Microbiology*. 2015 May 1;23(5):257–66.
25. Berg HC. *E. coli in motion*. New York: Springer; 2004. 133 p. (Biological and medical physics series).
26. Bialek W, Setayeshgar S. Physical limits to biochemical signaling. *PNAS*. 2005 Jul 19;102(29):10040–5.
27. Kaizu K, de Ronde W, Paijmans J, Takahashi K, Tostevin F, ten Wolde PR. The Berg-Purcell Limit Revisited. *Biophysical Journal*. 2014 Feb 18;106(4):976–85.
28. ten Wolde PR, Becker NB, Ouldrige TE, Mugler A. Fundamental Limits to Cellular Sensing. *J Stat Phys*. 2016 Mar 1;162(5):1395–424.
29. Endres RG, Wingreen NS. Maximum Likelihood and the Single Receptor. *Phys Rev Lett*. 2009 Oct 7;103(15):158101.
30. Mehta P, Schwab DJ. Energetic costs of cellular computation. *PNAS*. 2012 Oct 30;109(44):17978–82.
31. Lang AH, Fisher CK, Mora T, Mehta P. Thermodynamics of Statistical Inference by Cells. *Phys Rev Lett*. 2014 Oct 3;113(14):148103.
32. Govern CC, ten Wolde PR. Energy Dissipation and Noise Correlations in Biochemical Sensing. *Phys Rev Lett*. 2014 Dec 16;113(25):258102.

33. Mora T, Nemenman I. Physical Limit to Concentration Sensing in a Changing Environment. *Phys Rev Lett*. 2019 Nov 5;123(19):198101.
34. Malaguti G, ten Wolde PR. Receptor time integration via discrete sampling. *Phys Rev E*. 2022 May 11;105(5):054406.
35. Mora T, Wingreen NS. Limits of Sensing Temporal Concentration Changes by Single Cells. *Phys Rev Lett*. 2010 Jun 14;104(24):248101.
36. Hein AM, Brumley DR, Carrara F, Stocker R, Levin SA. Physical limits on bacterial navigation in dynamic environments. *Journal of The Royal Society Interface*. 2016 Jan 31;13(114):20150844.
37. Aquino G, Wingreen NS, Endres RG. Know the Single-Receptor Sensing Limit? Think Again. *J Stat Phys*. 2016 Mar 1;162(5):1353–64.
38. Cover TM, Thomas JA. *Elements of Information Theory*. New York, NY: Wiley-Interscience; 1991.
39. Sigtermans D. Towards a Framework for Observational Causality from Time Series: When Shannon Meets Turing. *Entropy*. 2020 Apr;22(4):426.
40. Schreiber T. Measuring Information Transfer. *Phys Rev Lett*. 2000 Jul 10;85(2):461–4.
41. Shannon CE. A Mathematical Theory of Communication. *Bell System Technical Journal*. 1948;27(3):379–423.
42. Bialek W, Nemenman I, Tishby N. Predictability, complexity, and learning. *Neural Comput*. 2001 Nov;13(11):2409–63.
43. Bialek W, De Ruyter Van Steveninck RR, Tishby N. Efficient representation as a design principle for neural coding and computation. In: 2006 IEEE International Symposium on Information Theory. 2006. p. 659–63.
44. Becker NB, Mugler A, ten Wolde PR. Optimal Prediction by Cellular Signaling Networks. *Phys Rev Lett*. 2015 Dec 17;115(25):258103.
45. Palmer SE, Marre O, Berry MJ, Bialek W. Predictive information in a sensory population. *PNAS*. 2015 Jun 2;112(22):6908–13.
46. Sachdeva V, Mora T, Walczak AM, Palmer SE. Optimal prediction with resource constraints using the information bottleneck. *PLOS Computational Biology*. 2021 Mar 8;17(3):e1008743.
47. Wang S, Segev I, Borst A, Palmer S. Maximally efficient prediction in the early fly visual system may support evasive flight maneuvers. *PLOS Computational Biology*. 2021 May 20;17(5):e1008965.
48. Tjalma AJ, Galstyan V, Goedhart J, Slim L, Becker NB, Wolde PR ten. Trade-offs between cost and information in cellular prediction [Internet]. *bioRxiv*; 2023 [cited 2023 Jan 12]. p. 2023.01.10.523390. Available from: <https://www.biorxiv.org/content/10.1101/2023.01.10.523390v1>

49. Lovely PS, Dahlquist FW. Statistical measures of bacterial motility and chemotaxis. *Journal of Theoretical Biology*. 1975 Apr 1;50(2):477–96.
50. Kolmogorov AN. Interpolation and Extrapolation of Stationary Sequences. *Izvestiya the Academy of Sciences of the USSR*. 1941;5:3–14.
51. Kolmogorov AN. Stationary sequences in Hilbert space. *Bull Moscow Univ*. 1941;2(6):1–40.
52. Wiener N. *Extrapolation, Interpolation, and Smoothing of Stationary Time Series: With Engineering Applications*. Cambridge, MA, USA: MIT Press; 1949. 163 p.
53. Andrews BW, Yi TM, Iglesias PA. Optimal Noise Filtering in the Chemotactic Response of *Escherichia coli*. *PLOS Computational Biology*. 2006 Nov 17;2(11):e154.
54. Hinczewski M, Thirumalai D. Cellular Signaling Networks Function as Generalized Wiener-Kolmogorov Filters to Suppress Noise. *Phys Rev X*. 2014 Oct 29;4(4):041017.
55. Husain K, Pittayakanchit W, Pattanayak G, Rust MJ, Murugan A. Kalman-like Self-Tuned Sensitivity in Biophysical Sensing. *Cell Systems*. 2019 Nov;9(5):459-465.e6.
56. Segall JE, Block SM, Berg HC. Temporal comparisons in bacterial chemotaxis. *PNAS*. 1986 Dec 1;83(23):8987–91.
57. Korobkova E, Emonet T, Vilar JMG, Shimizu TS, Cluzel P. From molecular noise to behavioural variability in a single bacterium. *Nature*. 2004 Apr;428(6982):574–8.
58. Colin R, Rosazza C, Vaknin A, Sourjik V. Multiple sources of slow activity fluctuations in a bacterial chemosensory network. Barkai N, editor. *eLife*. 2017 Dec 12;6:e26796.
59. Keegstra JM, Kamino K, Anquez F, Lazova MD, Emonet T, Shimizu TS. Phenotypic diversity and temporal variability in a bacterial signaling network revealed by single-cell FRET. Barkai N, editor. *eLife*. 2017 Dec 12;6:e27455.
60. Francis NR, Levit MN, Shaikh TR, Melanson LA, Stock JB, DeRosier DJ. Subunit Organization in a Soluble Complex of Tar, CheW, and CheA by Electron Microscopy. *J Biol Chem*. 2002 Sep 27;277(39):36755–9.
61. Levit MN, Grebe TW, Stock JB. Organization of the Receptor-Kinase Signaling Array That Regulates *Escherichia coli* Chemotaxis. *J Biol Chem*. 2002 Sep 27;277(39):36748–54.
62. Yang Y, M. Pollard A, Höfler C, Poschet G, Wirtz M, Hell R, et al. Relation between chemotaxis and consumption of amino acids in bacteria. *Molecular Microbiology*. 2015;96(6):1272–82.
63. Spudich JL, Koshland DE. Non-genetic individuality: chance in the single cell. *Nature*. 1976 Aug;262(5568):467–71.
64. Park H, Pontius W, Guet CC, Marko JF, Emonet T, Cluzel P. Interdependence of behavioural variability and response to small stimuli in bacteria. *Nature*. 2010 Dec;468(7325):819–23.

65. Park H, Oikonomou P, Guet CC, Cluzel P. Noise Underlies Switching Behavior of the Bacterial Flagellum. *Biophysical Journal*. 2011 Nov 16;101(10):2336–40.
66. Masson JB, Voisinne G, Wong-Ng J, Celani A, Vergassola M. Noninvasive inference of the molecular chemotactic response using bacterial trajectories. *PNAS*. 2012 Jan 31;109(5):1802–7.
67. Dufour YS, Gillet S, Frankel NW, Weibel DB, Emonet T. Direct Correlation between Motile Behavior and Protein Abundance in Single Cells. *PLOS Computational Biology*. 2016 Sep 6;12(9):e1005041.
68. Waite AJ, Frankel NW, Dufour YS, Johnston JF, Long J, Emonet T. Non-genetic diversity modulates population performance. *Molecular Systems Biology*. 2016 Dec 1;12(12):895.
69. Fu X, Kato S, Long J, Mattingly HH, He C, Vural DC, et al. Spatial self-organization resolves conflicts between individuality and collective migration. *Nature Communications*. 2018 Jun 5;9(1):2177.
70. Kamino K, Keegstra JM, Long J, Emonet T, Shimizu TS. Adaptive tuning of cell sensory diversity without changes in gene expression. *Science Advances*. 2020;
71. Kamino K, Kadakia N, Aoki K, Shimizu TS, Emonet T. Optimal inference of molecular interactions in live FRET imaging [Internet]. *bioRxiv*; 2022 [cited 2022 Aug 20]. p. 2022.03.29.486267. Available from: <https://www.biorxiv.org/content/10.1101/2022.03.29.486267v1>
72. Moore JP, Kamino K, Kottou R, Shimizu TS, Emonet T. Signal integration and adaptive sensory diversity tuning in *Escherichia coli* chemotaxis. *Cell Systems*. 2024;15.
73. Sourjik V, Berg HC. Receptor sensitivity in bacterial chemotaxis. *Proceedings of the National Academy of Sciences*. 2002 Jan 8;99(1):123–7.
74. Sourjik V, Berg HC. Functional interactions between receptors in bacterial chemotaxis. *Nature*. 2004 Mar;428(6981):437–41.
75. Monod J, Wyman J, Changeux JP. On the nature of allosteric transitions: A plausible model. *Journal of Molecular Biology*. 1965 May 1;12(1):88–118.
76. Mello BA, Tu Y. An allosteric model for heterogeneous receptor complexes: Understanding bacterial chemotaxis responses to multiple stimuli. *PNAS*. 2005 Nov 29;102(48):17354–9.
77. Keymer JE, Endres RG, Skoge M, Meir Y, Wingreen NS. Chemosensing in *Escherichia coli*: Two regimes of two-state receptors. *PNAS*. 2006 Feb 7;103(6):1786–91.
78. Moore JP, Kamino K, Emonet T. Non-Genetic Diversity in Chemosensing and Chemotactic Behavior. *International Journal of Molecular Sciences*. 2021 Jan;22(13):6960.
79. Kalinin YV, Jiang L, Tu Y, Wu M. Logarithmic Sensing in *Escherichia coli* Bacterial Chemotaxis. *Biophysical Journal*. 2009 Mar 18;96(6):2439–48.
80. Lazova MD, Ahmed T, Bellomo D, Stocker R, Shimizu TS. Response rescaling in bacterial chemotaxis. *PNAS*. 2011 Aug 16;108(33):13870–5.

81. Adler M, Alon U. Fold-change detection in biological systems. *Current Opinion in Systems Biology*. 2018 Apr 1;8:81–9.
82. Sarkka S. *Bayesian Filtering and Smoothing* [Internet]. Cambridge: Cambridge University Press; 2013 [cited 2020 Jun 30]. Available from: <http://ebooks.cambridge.org/ref/id/CBO9781139344203>
83. Khursigara CM, Lan G, Neumann S, Wu X, Ravindran S, Borgnia MJ, et al. Lateral density of receptor arrays in the membrane plane influences sensitivity of the *E. coli* chemotaxis response. *EMBO J*. 2011 May 4;30(9):1719–29.
84. Hazel JR, Sidell BD. A method for the determination of diffusion coefficients for small molecules in aqueous solution. *Analytical Biochemistry*. 1987 Nov 1;166(2):335–41.
85. Cremer J, Segota I, Yang C yu, Arnoldini M, Sauls JT, Zhang Z, et al. Effect of flow and peristaltic mixing on bacterial growth in a gut-like channel. *PNAS*. 2016 Oct 11;113(41):11414–9.
86. Sartori P, Tu Y. Free Energy Cost of Reducing Noise while Maintaining a High Sensitivity. *Phys Rev Lett*. 2015 Sep 8;115(11):118102.
87. Mehta P, Lang AH, Schwab DJ. Landauer in the age of synthetic biology: energy consumption and information processing in biochemical networks. *J Stat Phys*. 2016 Mar;162(5):1153–66.
88. Hathcock D, Yu Q, Mello BA, Amin DN, Hazelbauer GL, Tu Y. A nonequilibrium allosteric model for receptor-kinase complexes: The role of energy dissipation in chemotaxis signaling. *Proceedings of the National Academy of Sciences*. 2023 Oct 17;120(42):e2303115120.
89. Hathcock D, Yu Q, Tu Y. Time-reversal symmetry breaking in the chemosensory array: asymmetric switching and dissipation-enhanced sensing [Internet]. arXiv; 2023 [cited 2024 Jan 10]. Available from: <http://arxiv.org/abs/2312.17424>
90. Sherry DM, Graf IR, Bryant SJ, Emonet T, Machta BB. Lattice ultrasensitivity produces large gain in *E. coli* chemosensing [Internet]. bioRxiv; 2024 [cited 2024 Jun 14]. p. 2024.05.28.596300. Available from: <https://www.biorxiv.org/content/10.1101/2024.05.28.596300v1>
91. Adler J. Chemotaxis in Bacteria. *Science*. 1966 Aug 12;153(3737):708–16.
92. de Gennes PG. Chemotaxis: the role of internal delays. *Eur Biophys J*. 2004 Dec 1;33(8):691–3.
93. Wong-Ng J, Melbinger A, Celani A, Vergassola M. The Role of Adaptation in Bacterial Speed Races. *PLOS Computational Biology*. 2016 Jun 3;12(6):e1004974.
94. Phan TV, Mattingly HH, Vo L, Marvin JS, Looger LL, Emonet T. Direct measurement of dynamic attractant gradients reveals breakdown of the Patlak–Keller–Segel chemotaxis model. *Proceedings of the National Academy of Sciences*. 2024 Jan 16;121(3):e2309251121.
95. Narla AV, Cremer J, Hwa T. A traveling-wave solution for bacterial chemotaxis with growth. *Proceedings of the National Academy of Sciences*. 2021 Nov 30;118(48):e2105138118.

Supplementary Information for: *E. coli* do not count single molecules

Henry H. Mattingly^{†,1}, Keita Kamino^{†,2}, Jude Ong^{‡,3}, Rafaela Kottou^{‡,3}, Thierry Emonet^{*,3,4,5}, Benjamin B. Machta^{*,4,5}

¹ Center for Computational Biology, Flatiron Institute

² Institute of Molecular Biology, Academia Sinica

³ Molecular, Cellular, and Developmental Biology, ⁴ Physics, and ⁵ QBio Institute, Yale University

† These authors contributed equally.

‡ These authors contributed equally.

* Correspondence to: Benjamin.machta@yale.edu; Thierry.emonet@yale.edu.

Contents

Supplementary figures.....	1
Background: Drift speed and information rate.....	3
Equivalence between transfer entropy and predictive information rates.....	4
Derivation of the information in particle arrivals.....	5
Optimal kernel for estimating signal from particle arrivals.....	11
Modeling kinase activity.....	13
Derivation of the behaviorally-relevant information rate in kinase activity.....	14
Optimal kernel for estimating signal from kinase activity.....	19
Information about current versus past signals encoded in kinase activity.....	20
Appendix A: Causal Wiener filter derivation.....	22
Supplemental References.....	25

Supplementary figures

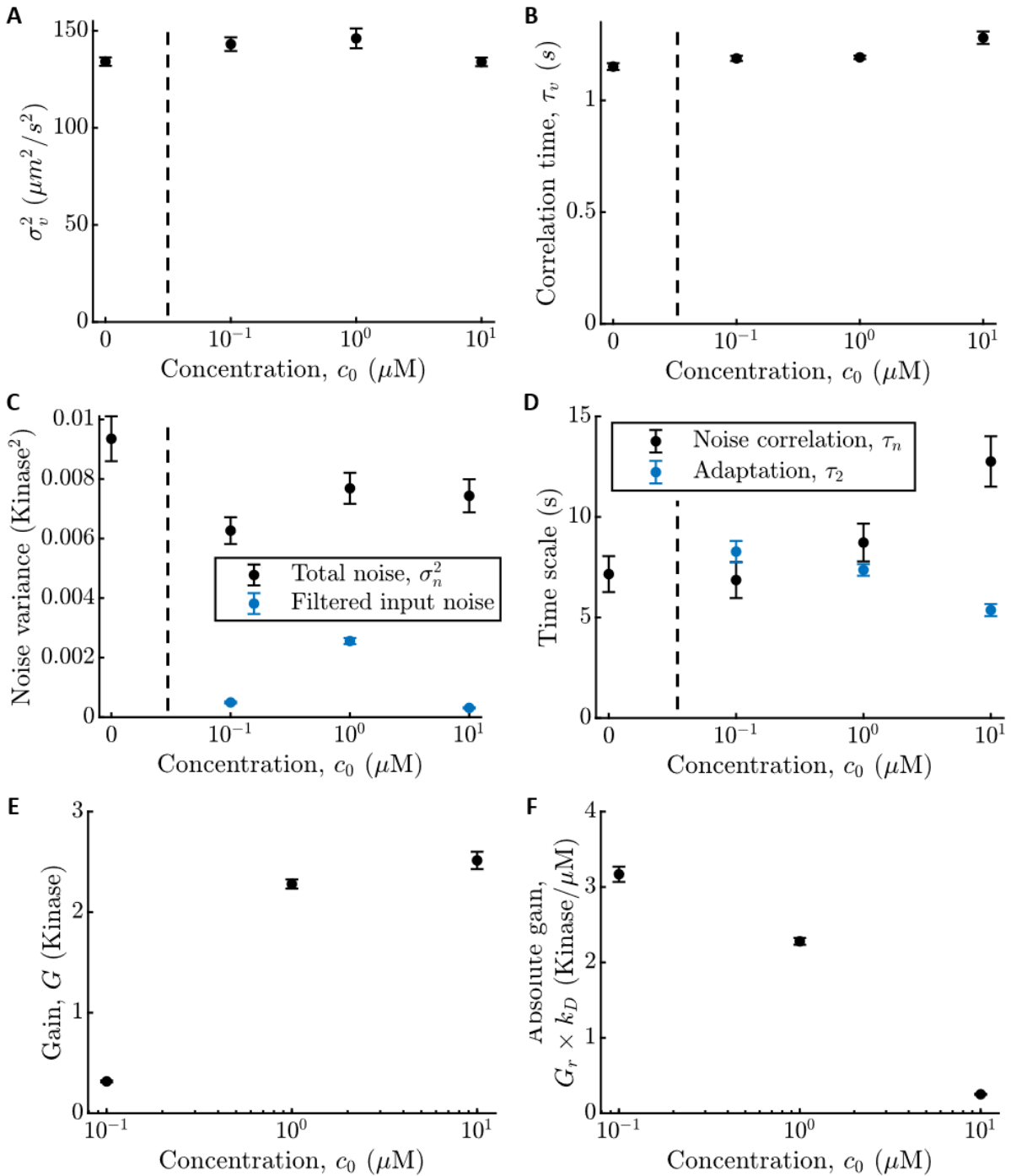


Fig. S1: Measured signal, response, and noise parameter values in different background concentrations.

A) Estimated variance of up-gradient velocity, σ_v^2 , as a function of background c_0 , which together with the gradient steepness g sets the signal strength. Horizontal axes are on log-scale, and vertical dashed lines throughout separate parameters measured at $c_0 = 0$ from those measured at finite c_0 . Error bars

throughout are standard error of the mean (see Methods in the main text). **B**) Correlation time of up-gradient velocity, τ_v , which sets the signal correlation time. Parameters in (A) and (B) are those of the median phenotype in Fig. S2, with tumble bias $TB \approx 0.09$. **C**) Variance of the total noise in kinase activity, σ_n^2 (black), and the estimated variance of particle arrival noise filtered through the kinase response kernel (blue) with $\tau_1 = 1/60$ s (1,2). **D**) Kinase noise correlation time, τ_n , and kinase response adaptation time, τ_2 (blue). **E**) Gain of kinase response to signal or log-concentration, G . **D**) Gain of kinase response to absolute concentration, $G_c = k_D G_r = G/c_0$, where G_r is the gain of kinase responses to particle arrival rate.

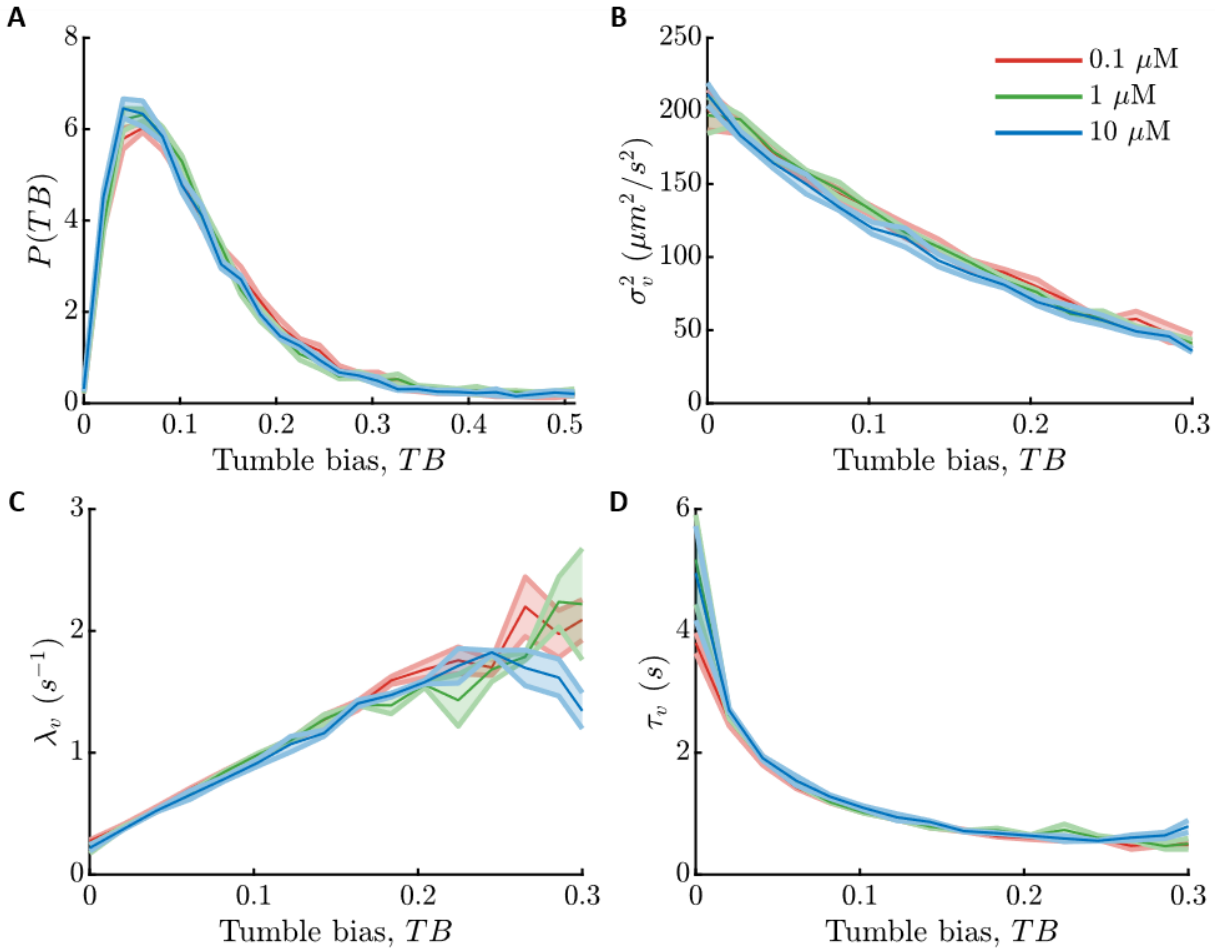


Fig. S2: Swimming parameters as a function of tumble bias in different background concentrations. A) Distribution of tumble bias, $TB = 1 - P_{run}$, or fraction of time cells spend in the tumble state, among cells in an isogenic population. Throughout: red is $c_0 = 0.1 \mu\text{M}$, green is $c_0 = 1 \mu\text{M}$, and blue is $c_0 = 10 \mu\text{M}$. Shading is standard error of the mean (Methods). **B**) Variance of up-gradient velocity, σ_v^2 , versus tumble bias, TB . **C**) Velocity decorrelation rate, $\lambda_v = \tau_v^{-1} \approx (1 - \alpha) \lambda_{R0} + 2 D_r$, versus TB . α quantifies how correlated heading is before and after a tumble; λ_{R0} is the average tumble rate; and D_r is the rotational diffusion coefficient (3). **D**) Velocity correlation time, τ_v .

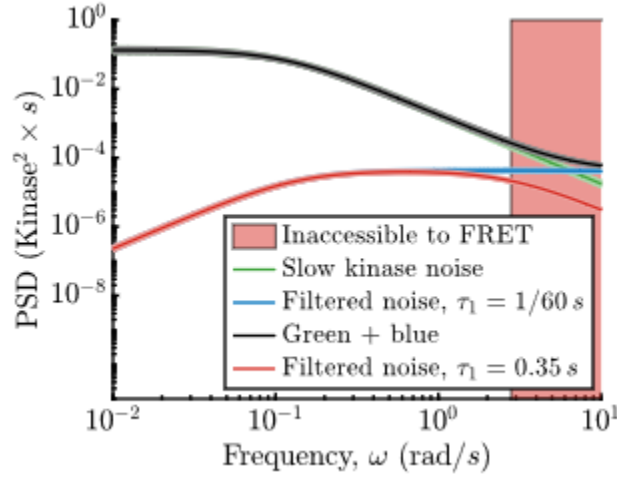


Fig. S3: Noise power spectra. In frequency space, kinase responses to particle arrivals implies that the noise in kinase activity must be larger than filtered particle arrival noise (blue, using $\tau_1 = 1/60$ s from biochemistry studies Refs. (1,2)). At low frequencies where we can measure noise and responses with our FRET system (green), this bound is far from saturated. Naively extrapolating to higher frequencies (red shaded region, marked by the value of $1/\tau_1$ measured in FRET experiments) violates this bound (the green line goes below the blue line). This implies either additional noise at high frequencies that is not captured by a single exponential (black line is slow noise, green, plus filtered particle noise, blue) or a slower kinase response time τ_1 (red line is filtered particle noise with $\tau_1 \approx 0.35$ s measured in FRET experiments), which could be a necessary by product of the coupling between kinases that creates large gain (thus raising the red line) but also slows down the response. The behaviorally-relevant information rates computed in the main text are relatively insensitive to these choices.

Background: Drift speed and information rate

We recently demonstrated that a cell's drift speed v_d is set by the transfer entropy rate, $\dot{I}_{s \rightarrow m}^*$, from current signal $s(t) = \frac{1}{c_0} \frac{dc}{dt}$ to (the trajectory of) swimming behavior $m(t)$ (3). The transfer entropy rate from current signal to swimming behavior is defined as:

$$\dot{I}_{s \rightarrow m}^* = \lim_{dt \rightarrow 0} \frac{1}{dt} I(m(t+dt); s(t) | \{m(t)\}) \quad (1)$$

$$= \lim_{dt \rightarrow 0} \frac{1}{dt} \left\langle \log \left(\frac{P(m(t+dt) | s(t), \{m(t)\})}{P(m(t+dt) | \{m(t)\})} \right) \right\rangle. \quad (2)$$

Here, curly brackets denote the entire past of a variable, up to and including time t . Angled brackets indicate an averaged over the joint distribution of $s(t)$, past $m(t)$, and $m(t+dt)$. This quantifies how strongly the swimming transition probabilities depend on the current signal.

The transfer entropy rate from current signal determines the cell's drift speed (3):

$$\frac{v_d}{v_0} = \frac{(1 - \alpha) \lambda_{R0}}{(1 - \alpha) \lambda_{R0} + 2 D_r} \left(\frac{2 \dot{I}_{s \rightarrow m}^* P_{run}}{3 \lambda_{R0}} \right)^{1/2} \quad (3)$$

where v_0 is the cell's swimming speed, λ_{R0} is the cell's average tumble rate, α is the persistence of the cell's orientation upon tumbling, D_r is the rotational diffusion coefficient, and P_{run} is the fraction of time the cell spends in the run state.

This transfer entropy obeys a series of data processing inequalities (4,5) because of the feed-forward relationship between molecule arrival rate $r(t)$, kinase activity $a(t)$, and swimming behavior $m(t)$:

$$\dot{I}_{s \rightarrow r}^* \geq \dot{I}_{s \rightarrow a}^* \geq \dot{I}_{s \rightarrow m}^*. \quad (4)$$

Thus, information about current signal available in particle arrivals sets a fundamental upper limit on a cell's gradient climbing speed. Because these information rates set the cell's chemotaxis performance, defined as v_d/v_0 , these transfer entropy rates quantify behaviorally-relevant information.

Equivalence between transfer entropy and predictive information rates

Here we demonstrate that the transfer entropy rates above are equivalent to a predictive information rate, under some assumptions that are satisfied by bacterial chemotaxis. This relationship is useful because it allows us to derive expressions for the behaviorally-relevant information rates above.

Below, we will write transfer entropy rate from a signal $s(t)$ to a stochastic process $x(t)$, such as $r(t)$, $a(t)$, or $m(t)$. Starting from the definition above:

$$\dot{I}_{s \rightarrow x}^* = \lim_{dt \rightarrow 0} \frac{1}{dt} I(x(t + dt); s(t) | \{x(t)\}), \quad (5)$$

conditional mutual information can always be written as a difference between two unconditioned mutual information terms:

$$= \lim_{dt \rightarrow 0} \frac{1}{dt} \left(I(\{x(t + dt)\}; s(t)) - I(\{x(t)\}; s(t)) \right). \quad (6)$$

This can be written as

$$= [\partial_T I(\{x(T)\}; s(t))]_{T=t}. \quad (7)$$

Changing variables from T to τ , where $T = t + \tau$, we get:

$$= [\partial_\tau I(\{x(t + \tau)\}; s(t))]_{\tau=0}. \quad (8)$$

Next, we use time stationarity to shift time t by $-\tau$:

$$= [\partial_\tau I(\{x(t)\}; s(t - \tau))]_{\tau=0}. \quad (9)$$

Finally, we can change variables to $\tau \rightarrow -\tau$, giving:

$$= -[\partial_\tau I(\{x(t)\}; s(t + \tau))]_{\tau=0}. \quad (10)$$

This last step would not be allowed if the mutual information inside the time derivative was the entire past of s , i.e. $\{s(t + \tau)\}$.

Inside the time derivative above is the “predictive information” (6–8) between the entire past of the stochastic process $x(t)$ up to time t and the signal $s(t)$ at some time τ into the future (if $\tau > 0$). The time derivative of this mutual information or predictive information is a monotonically decreasing function of τ : the value of the signal s at a time further in the future (larger τ) becomes less correlated with past observations and thus harder to predict.

Derivation of the information in particle arrivals

In this section we derive the information rate from current signal $s(t)$ to past particle counts r , which sets a fundamental upper limit on the information rate achievable by a cell. This information rate is given by the following transfer entropy rate:

$$\begin{aligned} i_{s \rightarrow r}^* &= \lim_{dt \rightarrow 0} \frac{1}{dt} I(r(t + dt); s(t) | \{r(t)\}) \\ &= -[\partial_\tau I(\{r(t)\}; s(t + \tau))]_{\tau=0}. \end{aligned} \quad (11)$$

Here, $s(t) = \frac{d}{dt} \log(c)$ is the relative rate of change of ligand concentration along the cell’s trajectory, and $r(t)$ is the number of ligand molecules per time that arrive at the cell’s surface.

The key quantity we need to derive is the mutual information inside of the derivative:

$$I(\{r(t)\}; s(t + \tau)) = \left\langle \log \left(\frac{P(s(t + \tau) | \{r(t)\})}{P(s(t + \tau))} \right) \right\rangle = \left\langle \log \left(\frac{P(\{r(t)\} | s(t + \tau))}{P(\{r(t)\})} \right) \right\rangle. \quad (12)$$

In general, it is difficult to derive the conditional distributions above. However, we can make a few simplifying assumptions. First, although the distribution of particle arrival rate $P(\{r(t)\} | s(t + \tau))$ has Poisson statistics, if a sufficient number of particles arrive at the cell’s receptor array per unit time, the Poisson statistics are approximately Gaussian. This approximation is accurate when the cell sees much more than 1 particle per run on average.

Even with this approximation, $P(\{r(t)\}) = \int P(\{r(t)\} | s(t + \tau)) P(s(t + \tau)) ds$ is technically not Gaussian because $P(s(t + \tau))$ is not Gaussian. However, in shallow gradients (small s), the (roughly) Gaussian particle arrival noise described by $P(\{r(t)\} | s(t + \tau))$ blurs the structure in $P(s(t + \tau))$, making $P(\{r(t)\})$ nearly Gaussian, as well. As a result, we can approximate the mutual information in Eqn. 12 by approximating all distributions as Gaussian, as shown rigorously by others (9–11).

We focus on computing a Gaussian approximation of $P(s(t + \tau) | \{r(t)\})$. For this, we only need to compute the mean $\mu_{s|r}(\tau)$ and variance $\sigma_{s|r}^2(\tau)$. The mutual information can then be computed from:

$$I(\{r(t)\}; s(t + \tau)) \approx \frac{1}{2} \log \left(\frac{\sigma_s^2}{\sigma_{s|r}^2(\tau)} \right) = -\frac{1}{2} \log(1 - \rho_{rs}^2(\tau)), \quad (13)$$

and the information rate is:

$$\dot{I}_{s \rightarrow r}^* = \frac{1}{2} \left[\frac{-\partial_\tau \rho_{rs}^2(\tau)}{1 - \rho_{rs}^2(\tau)} \right]_{\tau=0}. \quad (14)$$

Here, σ_s^2 is the marginal variance of $s(t + \tau)$ or $s(t)$, i.e. the variance of the distribution $P(s(t + \tau)) = P(s(t))$ (by time-translation invariance). Then, $\rho_{rs}^2(\tau) = 1 - \frac{\sigma_{s|r}^2(\tau)}{\sigma_s^2}$ is a generalized correlation coefficient between $s(t + \tau)$ and past r , or the fraction reduction of variance in $s(t + \tau)$ upon observing past r .

To determine $\dot{I}_{s \rightarrow r}^*$, we now need to calculate the generalized correlation coefficient $\rho_{rs}^2(\tau)$ using models for the dynamics of s and r . Consider a single cell navigating a shallow, static chemical gradient, $c(x) = c_0 e^{g x} \sim c_0(1 + g x)$, that varies along one spatial dimension, x , in 3D space. In a static gradient, the signal is determined by the cell's motion in the gradient: $s(t) = \frac{d}{dt} \log(c) \approx \frac{1}{c_0} \frac{dc}{dt} = g v_x(t)$. As done before (3), we model the cell's up-gradient velocity, and thus the signal, as a Gaussian process with correlation function:

$$\langle s(t) s(t') \rangle = g^2 V(t) = g^2 \sigma_v^2 \exp\left(-\frac{|t - t'|}{\tau_v}\right). \quad (15)$$

Here, $\sigma_v^2 \approx \frac{v_0^2}{3} P_{run}$ is the variance of the cell's up-gradient velocity, v_0 is its swimming speed, and P_{run} is the fraction of time it spends in the run state; and τ_v is the correlation time of the cell's velocity and the signal, $\tau_v^{-1} = (1 - \alpha) \lambda_{R0} + 2 D_r$, where λ_{R0} is the cell's baseline tumble rate, α is the directional persistence, and D_r is the rotational diffusion coefficient.

Then, concentration and particle arrival rate can be modeled as:

$$\frac{dc}{dt} = c_0 s(t) \quad (16)$$

$$r(t) = k_D c(t) + \sqrt{r_0} \xi(t). \quad (17)$$

$k_D = 4 D l$ is the diffusion-limited rate constant of particle arrivals to a membrane patch of radius l and for ligand diffusion coefficient D (12–14). The particle arrival noise obeys $\langle \xi(t) \xi(t') \rangle = \delta(t - t')$, and $r_0 = k_D c_0$ is the particle arrival rate in background concentration c_0 .

Since all distributions are approximately Gaussian, the posterior distribution of $s(t + \tau)$ given past $r(t)$ is Gaussian as well: $p(s(t + \tau) | \{r(t)\}) = \mathcal{N}(\mu_{s|r}(\tau), \sigma_{s|r}^2(\tau))$. The mean of this distribution, $\mu_{s|r}(\tau)$, can be computed using the causal Wiener filter, $M_r(T)$, which minimizes the following mean squared error $\langle e^2(\tau) \rangle$:

$$\langle e^2(\tau) \rangle = \left\langle \left(s(t + \tau) - \int_{-\infty}^t M_r(t - t') r(t') dt' \right)^2 \right\rangle \quad (18)$$

Once the optimal kernel $M_r(T)$ is obtained, the mean of the posterior is $\mu_{s|r}(\tau) = \int_{-\infty}^t M_r(t - t') r(t') dt'$ and the variance is $\sigma_{s|r}^2(\tau) = \langle e^2(\tau) \rangle$. Therefore, to derive the mutual information $I(\{r(t)\}; s(t + \tau))$, and thus the information rate $\dot{I}_{s \rightarrow r}^*$, we need to derive this Wiener filter. The main challenge in deriving $M_r(T)$ is that it must satisfy the constraint that it is causal: that is, we require that

$M_r(T) = 0$ for $T < 0$. In Appendix A, we derive the necessary equations and explain where they come from, but here we will just apply them to get $M_r(t)$. See also references (8,15,16).

The optimal kernel can be expressed in Fourier space terms of the power spectra of the signal $s(t)$ and the particle arrival rate $r(t)$ as (Appendix A):

$$M_r(\omega) = \frac{1}{\phi_r(\omega)} \left[\frac{S_{rs}(\omega)}{\phi_r^*(\omega)} e^{-i\omega\tau} \right]^+ . \quad (19)$$

$M_r(\omega)$ is the Fourier transform of $M_r(T)$, with the Fourier transform defined as $F[f(t)] = \int_{-\infty}^{\infty} f(t) e^{i\omega t} dt$ and inverse transform defined as $F^{-1}[f(\omega)] = \frac{1}{2\pi} \int_{-\infty}^{\infty} f(\omega) e^{-i\omega t} d\omega$. $\phi_r(\omega)$ is the causal part of the spectral decomposition of $S_r(\omega)$ (defined below and in Appendix A), where $S_r(\omega)$ is the power spectrum of r . $\phi_r^*(\omega)$ is its (anti-causal) complex conjugate. $S_{rs}(\omega)$ is the cross-spectra of r and s , equivalent to the Fourier transform of $C_{rs}(\tau)$, where $C_{rs}(\tau) = \langle (r(t) - r_0)s(t + \tau) \rangle$ is the cross-correlation of s and r in the time domain. Finally, $[f(\omega)]^+$ indicates the causal part of the inverse Fourier transform of $f(\omega)$, which can be found by taking the inverse Fourier transform of $f(\omega)$, multiplying the result by a Heaviside step function in the time domain, and then taking the Fourier transform.

To derive these various quantities, we take the Fourier transforms of Eqns. 16 and 17, and then solve for the Fourier transforms of our variables $c(\omega)$ and $r(\omega)$:

$$c(\omega) = \frac{c_0}{\frac{\epsilon}{\tau_v} - i\omega} s(\omega) \quad (20)$$

$$r(\omega) = k_D c(\omega) + \sqrt{r_0} \xi(\omega). \quad (21)$$

Here we have introduced a small, dimensionless parameter $\epsilon \ll 1$ that we will take to zero later. Physically, this is as if the cell experiences a weak restoring force back to regions where concentration $c(x) = c_0$. Without it, the correlation function of $c(t)$, which is proportional to the cell's mean squared displacement, would diverge at long times. Everything else remains bounded and well-defined as ϵ goes to zero.

From these and the correlation function of $s(t)$, we derive the following spectra:

$$S_s(\omega) = F[C_s(T)] = \frac{2g^2 \frac{\sigma_v^2}{\tau_v}}{\frac{1}{\tau_v^2} + \omega^2} \quad (22)$$

$$S_r(\omega) = F[C_r(T)] = \frac{r_0^2}{\frac{\epsilon^2}{\tau_v^2} + \omega^2} S_s(\omega) + r_0 \quad (23)$$

$$S_{rs}(\omega) = S_{sr}^*(\omega) = F[C_{rs}(T)] = \frac{r_0}{\frac{\epsilon}{\tau_v} + i\omega} S_s(\omega) \quad (24)$$

where $C_s(T) = \langle s(t) s(t + T) \rangle$, $C_r(T) = \langle (r(t) - r_0) (r(t + T) - r_0) \rangle$, and $C_{rs}(T) = \langle (r(t) - r_0) s(t + T) \rangle$.

As explained in Appendix A, to find the optimal causal kernel, we need to decompose $S_r(\omega)$ into the product of a causal and an anti-causal part. This requires finding the zeros and poles of $S_r(\omega)$. The zeros satisfy $S_r(\omega = i z_r) = 0$, and therefore are the complex solutions to the equation:

$$2 r_0 g^2 \sigma_v^2 \tau_v^3 + (\epsilon^2 + \tau_v^2 \omega^2) (1 + \tau_v^2 \omega^2) = 0 \quad (25)$$

or, defining $\gamma_r = 2 r_0 g^2 \sigma_v^2 \tau_v^3$:

$$\gamma_r + (\epsilon^2 + \tau_v^2 \omega^2) (1 + \tau_v^2 \omega^2) = 0. \quad (26)$$

γ_r is a dimensionless signal-to-noise ratio parameter, where the signal is $r_0^2 g^2 \sigma_v^2 \tau_v^3$ (the prefactor of the first term in $S_r(\omega)$ when ω is rescaled by $1/\tau_v$) and the noise is r_0 (the second term in $S_r(\omega)$).

The zeros of $S_r(\omega)$ are:

$$i z_{r,1} = i \frac{1}{\sqrt{2} \tau_v} \sqrt{1 + \epsilon^2 + \sqrt{(1 - \epsilon^2)^2 - 4 \gamma_r}}, \quad i z_{r,2} = i \frac{1}{\sqrt{2} \tau_v} \sqrt{1 + \epsilon^2 - \sqrt{(1 - \epsilon^2)^2 - 4 \gamma_r}}, \quad (27)$$

as well as their complex conjugates, z_1^* and z_2^* . As $\epsilon \rightarrow 0$, these will simplify to:

$$i z_{r,1} = i \frac{1}{\sqrt{2} \tau_v} \sqrt{1 + \sqrt{1 - 4 \gamma_r}}, \quad i z_{r,2} = i \frac{1}{\sqrt{2} \tau_v} \sqrt{1 - \sqrt{1 - 4 \gamma_r}}, \quad (28)$$

Note that there are several equivalent forms for these zeros, and they change from being fully imaginary to complex when $\gamma_r > 1/4$.

The poles of $S_r(\omega)$ satisfy $\frac{1}{S_r(\omega=i p_r)} = 0$ and are given by $i p_{r,1} = i \frac{\epsilon}{\tau_v}$ and $i p_{r,2} = i \frac{1}{\tau_v}$, as well as their complex conjugates $p_{r,1}^*$ and $p_{r,2}^*$.

Power spectral densities of real, stable, causal systems can generally be decomposed into causal and anti-causal parts ("Wiener-Hopf factorization") (17–19):

$$S_r(\omega) = \phi_r(\omega) \phi_r^*(\omega) \quad (29)$$

where

$$\phi_r(\omega) = \sqrt{r_0} \frac{(z_{r,1} - i \omega) (z_{r,2} - i \omega)}{(p_{r,1} - i \omega) (p_{r,2} - i \omega)} \quad (30)$$

has zeros and poles with negative imaginary parts, and $\phi_r^*(\omega)$ is its complex conjugate.

Next, we need the causal part of (see Appendix A):

$$\frac{S_{rS}(\omega)}{\phi_r^*(\omega)} e^{-i \omega \tau} = \frac{\sqrt{r_0}}{\frac{\epsilon}{\tau_v} + i \omega} S_s(\omega) \frac{(p_{r,1} + i \omega) (p_{r,2} + i \omega)}{(z_{r,1} + i \omega) (z_{r,2} + i \omega)} e^{-i \omega \tau} \quad (31)$$

$$= \frac{\sqrt{r_0}}{\frac{\epsilon}{\tau_v} + i \omega} \frac{2 g^2 \sigma_v^2}{\tau_v} \frac{(\frac{\epsilon}{\tau_v} + i \omega) (\frac{1}{\tau_v} + i \omega)}{(z_{r,1} + i \omega) (z_{r,2} + i \omega)} e^{-i \omega \tau} \quad (32)$$

$$= \sqrt{r_0} \frac{2 g^2 \frac{\sigma_v^2}{\tau_v}}{\left(\frac{1}{\tau_v} - i \omega\right) (z_{r,1} + i \omega) (z_{r,2} + i \omega)} e^{-i \omega \tau} \quad (33)$$

$$= \frac{\gamma_r}{\sqrt{r_0} \tau_v^4} \frac{1}{\left(\frac{1}{\tau_v} - i \omega\right) (z_{r,1} + i \omega) (z_{r,2} + i \omega)} e^{-i \omega \tau} \quad (34)$$

One approach would be to compute the inverse Fourier transform of $\frac{S_{rs}(\omega)}{\phi_r^*(\omega)}$, apply the time shift forward by τ implied by $e^{-i \omega \tau}$, multiply the result by a Heaviside step function $\Theta(T)$, and compute the Fourier transform of the result. An alternative approach is to compute the partial fraction decomposition of the expression above and keep only the terms with poles and zeros that have negative imaginary part:

$$\frac{S_{rs}(\omega)}{\phi_r^*(\omega)} e^{-i \omega \tau} = \frac{A}{\left(\frac{1}{\tau_v} - i \omega\right)} + \frac{B}{(z_{r,1} + i \omega)} + \frac{C}{(z_{r,2} + i \omega)} \quad (35)$$

for unknown A , B , and C . Only the pole of the first term ($\omega = -i \frac{1}{\tau_v}$) has negative imaginary part, so we only need to compute A to get the causal part of this expression. With some algebra, this is:

$$A = \left[\frac{\gamma_r}{\sqrt{r_0} \tau_v^4} \frac{1}{(z_{r,1} + i \omega) (z_{r,2} + i \omega)} e^{-i \omega \tau} \right]_{\omega = -i \frac{1}{\tau_v}} \quad (36)$$

$$= \frac{\gamma_r}{\sqrt{r_0} \tau_v^2} \frac{1}{(1 + \tau_v z_{r,1}) (1 + \tau_v z_{r,2})} e^{-\frac{\tau}{\tau_v}}, \quad (37)$$

and the causal part of $\frac{S_{rs}(\omega)}{\phi_r^*(\omega)} e^{-i \omega \tau}$ is then:

$$\left[\frac{S_{rs}(\omega)}{\phi_r^*(\omega)} e^{-i \omega \tau} \right]^+ = \frac{\gamma_r}{\sqrt{r_0} \tau_v^2} \frac{1}{(1 + \tau_v z_{r,1}) (1 + \tau_v z_{r,2})} \frac{1}{\left(\frac{1}{\tau_v} - i \omega\right)} e^{-\frac{\tau}{\tau_v}}. \quad (38)$$

Finally, the optimal kernel that computes the mean of $p(s(t + \tau)|\{r(t)\})$, $\mu_{s|r}(\tau)$, is (Appendix A):

$$M_r(\omega) = \frac{1}{\phi_r(\omega)} \left[\frac{S_{rs}(\omega)}{\phi_r^*(\omega)} e^{-i \omega \tau} \right]^+ \quad (39)$$

$$= e^{-\frac{\tau}{\tau_v}} \frac{\gamma_r}{r_0 \tau_v^2} \frac{1}{(1 + \tau_v z_{r,1}) (1 + \tau_v z_{r,2})} \frac{-i \omega}{(z_{r,1} - i \omega) (z_{r,2} - i \omega)}, \quad (40)$$

after taking ϵ to zero. We convert this kernel to the time domain and discuss its properties in the next section.

The variance of $p(s(t + \tau)|\{r(t)\})$, $\sigma_{s|r}^2(\tau)$, is (Appendix A, Eqn. 127):

$$\sigma_{s|r}^2(\tau) = \sigma_s^2 - \frac{1}{2\pi} \int_{-\infty}^{\infty} S_{rs}^*(\omega) e^{i \omega \tau} M_r(\omega) d\omega \quad (41)$$

$$= \sigma_s^2 \left(1 - e^{-2\frac{\tau}{\tau_v}} \frac{\gamma_r}{(1 + \tau_v z_{r,1})^2 (1 + \tau_v z_{r,2})^2} \right) \quad (42)$$

where we used $\sigma_s^2 = g^2 \sigma_v^2 = \gamma / (2 r_0 \tau_v^3)$. Then the correlation coefficient $\rho_{rs}^2(\tau)$ is:

$$\rho_{rs}^2(\tau) = 1 - \frac{\sigma_{s|r}^2(\tau)}{\sigma_s^2} = e^{-2\frac{\tau}{\tau_v}} \frac{\gamma_r}{(1 + \tau_v z_{r,1})^2 (1 + \tau_v z_{r,2})^2}. \quad (43)$$

Finally, using Eqn. 14 from above, we find that the behaviorally-relevant information available in particle counts is:

$$I_{s \rightarrow r}^* = \frac{1}{\tau_v} \frac{\rho_{rs}^2(\tau = 0)}{1 - \rho_{rs}^2(\tau = 0)} = \frac{1}{\tau_v} \frac{\frac{\gamma_r}{\left(1 + \frac{1}{\sqrt{2}} \sqrt{1 + \sqrt{1 - 4\gamma_r}}\right)^2 \left(1 + \frac{1}{\sqrt{2}} \sqrt{1 - \sqrt{1 - 4\gamma_r}}\right)^2}}{1 - \frac{\gamma_r}{\left(1 + \frac{1}{\sqrt{2}} \sqrt{1 + \sqrt{1 - 4\gamma_r}}\right)^2 \left(1 + \frac{1}{\sqrt{2}} \sqrt{1 - \sqrt{1 - 4\gamma_r}}\right)^2}}. \quad (44)$$

Expanding around small SNR γ gives:

$$I_{s \rightarrow r}^* \approx \frac{1}{\tau_v} \frac{\gamma_r}{4} = \frac{1}{2} r_0 g^2 \sigma_v^2 \tau_v^2. \quad (45)$$

Note that for small signals, Eqn. 44 can be written $I_{s \rightarrow r}^* \approx \frac{1}{\tau_v} \rho_{rs}^2(\tau = 0) \approx \frac{2}{\tau_v} I(\{r(t)\}; s(t))$.

The optimal kernel in the time domain and the information rate remain real when $\gamma_r > 1/4$, even though $z_{r,1}$ and $z_{r,2}$ become complex. In this regime, they can be written:

$$z_{r,1} = \frac{1}{2\tau_v} \left(\sqrt{2\sqrt{\gamma_r} + 1} - i\sqrt{2\sqrt{\gamma_r} - 1} \right), \quad z_{r,2} = \frac{1}{2\tau_v} \left(\sqrt{2\sqrt{\gamma_r} + 1} + i\sqrt{2\sqrt{\gamma_r} - 1} \right). \quad (46)$$

The optimal kernel in frequency space can be written:

$$M_r(\omega) = e^{-\frac{\tau}{\tau_v}} \frac{\gamma_r}{r_0 \tau_v^2} \frac{1}{(1 + \tau_v z_{r,1})(1 + \tau_v z_{r,2})} \frac{-i\omega}{(z_{r,1} - i\omega)(z_{r,2} - i\omega)} \quad (47)$$

$$= e^{-\frac{\tau}{\tau_v}} \frac{\gamma_r}{r_0 \tau_v^2} \frac{1}{\left(1 + \sqrt{1 + 2\sqrt{\gamma_r} + \sqrt{\gamma_r}}\right)} \frac{-i\omega}{(z_{r,1} - i\omega)(z_{r,2} - i\omega)}, \quad (48)$$

the correlation coefficient at $\tau = 0$ can be written:

$$\rho_{rs}^2(\tau = 0) = \frac{\gamma_r}{(1 + z_{r,1} \tau_v)^2 (1 + z_{r,2} \tau_v)^2} \quad (49)$$

$$= \frac{\gamma_r}{|1 + z_{r,1} \tau_v|^4} \quad (50)$$

$$= \frac{\gamma_r}{\left(1 + \sqrt{1 + 2\sqrt{\gamma_r}} + \sqrt{\gamma_r}\right)^2}, \quad (51)$$

and the information rate is:

$$\dot{i}_{s \rightarrow r}^* = \frac{1}{\tau_v} \frac{\frac{\gamma_r}{\left(1 + \sqrt{1 + 2\sqrt{\gamma_r}} + \sqrt{\gamma_r}\right)^2}}{1 - \frac{\gamma_r}{\left(1 + \sqrt{1 + 2\sqrt{\gamma_r}} + \sqrt{\gamma_r}\right)^2}}. \quad (52)$$

For small γ_r , this reduces again to Eqn. 45.

Optimal kernel for estimating signal from particle arrivals

To get the time-domain kernel mapping past particle arrival rate $r(t)$ to signal $s(t + \tau)$, $M_r(T)$, we take the inverse Fourier transform of $M_r(\omega)$, defined as $IFT[f(\omega)] = \frac{1}{2\pi} \int_{-\infty}^{\infty} f(\omega) e^{-i\omega t} d\omega$. $M_r(T)$ has the form of a sum of two exponentials, with real exponents when $\gamma_r \leq 1/4$ and complex ones when $\gamma_r > 1/4$. For $\gamma_r < 1/4$, the kernel in the time domain is:

$$M_r(T) = e^{-\frac{\tau}{\tau_v}} \frac{\gamma_r}{r_0 \tau_v^2} \frac{1}{(1 + z_{r,1} \tau_v)(1 + z_{r,2} \tau_v)} \frac{(z_{r,1} e^{-z_{r,1} T} - z_{r,2} e^{-z_{r,2} T})}{z_{r,1} - z_{r,2}} \Theta(T), \quad (53)$$

where $\Theta(T)$ is the Heaviside step function, indicating that the kernel is indeed causal.

The optimal kernel $M_r(T)$ essentially computes the time derivative of concentration, while also averaging out shot noise from particle arrivals. It has several notable features. First, it is biphasic and exhibits perfect adaptation, a hallmark of the chemotaxis pathway. Any derivative operation should adapt perfectly because it should only respond to *changes* in the input.

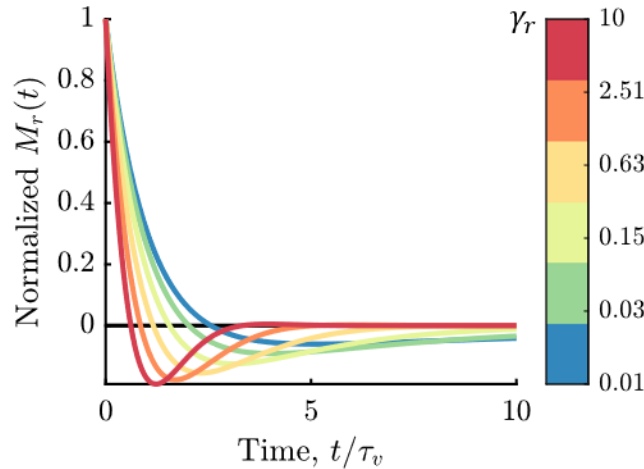


Fig. S4: Optimal kernel for inferring current signal, $s(t)$, from past particle arrivals, r . Colors indicate different values of the signal-to-noise ratio γ_r , marked on the right. Each kernel is normalized so that $M_r(0) = 1$.

It is interesting to examine how the time scales of the optimal kernel are set by the signal-to-noise ratio $\gamma_r = 2 r_0 g^2 \sigma_v^2 \tau_v^3$. The initial response time scale is set by $z_{r,1}^{-1}$ and its adaptation time scale is set by $z_{r,2}^{-1}$. When the inputs are very noisy, i.e. as $\gamma_r \rightarrow 0$, $z_{r,1}^{-1}$ gets longer but saturates at τ_v :

$$z_{r,1}^{-1}(\gamma_r \rightarrow 0) \approx \tau_v \left(1 - \frac{\gamma_r}{2}\right). \quad (54)$$

This makes sense because it maximally averages out shot noise, but only for as long as past signals are correlated with the current signal. As the SNR increases, this initial averaging time gets shorter.

As the inputs get noisier, i.e. as $\gamma_r \rightarrow 0$, the adaptation time approaches:

$$z_{r,2}^{-1}(\gamma_r \rightarrow 0) \approx \tau_v \left(\frac{1}{\sqrt{\gamma_r}} - \frac{\sqrt{\gamma_r}}{2}\right). \quad (55)$$

This shows that the adaptation time can become long compared to τ_v when $\gamma_r < 1/4$.

Interestingly, in this regime, the kernel $M_r(T)$ has the same functional form as the phenomenological kernel we measured previously (3) (after transforming the input quantity from $s(t)$ to $c(t)$).

When signal and noise have similar strength $\gamma_r = 1/4$, $z_{r,1} = z_{r,2} = z_r = \frac{1}{\sqrt{2}} \tau_v^{-1}$, and the optimal kernel becomes:

$$M_r(T) = e^{-\frac{T}{\tau_v}} \frac{\gamma_r}{r_0 \tau_v^2} \frac{1}{\left(1 + \frac{1}{\sqrt{2}}\right)^2} e^{-z_r T} (1 - z_r T) \Theta(T). \quad (56)$$

When SNR is high $\gamma_r > 1/4$, $z_{r,1}$ and $z_{r,2}$ become complex. However, since they are complex conjugates of each other, the kernel remains real:

$$\begin{aligned} M_r(T) &= e^{-\frac{T}{\tau_v}} \frac{\gamma_r}{r_0 \tau_v^2} \frac{1}{(1 + z_{r,1} \tau_v)(1 + z_{r,2} \tau_v)} e^{-\text{Re}[z_{r,2}] T} \left(\cos(\text{Im}[z_{r,2}] T) - \frac{\text{Re}[z_{r,2}]}{\text{Im}[z_{r,2}]} \sin(\text{Im}[z_{r,2}] T) \right) \Theta(T) \\ &= e^{-\frac{T}{\tau_v}} \frac{\gamma_r}{r_0 \tau_v^2} \frac{1}{\left(1 + \sqrt{1 + 2\sqrt{\gamma_r} + \sqrt{\gamma_r}}\right)} e^{-\frac{1}{2}\sqrt{2\sqrt{\gamma_r} + 1} \frac{T}{\tau_v}} \times \\ &\quad \left(\cos\left(\frac{1}{2}\sqrt{2\sqrt{\gamma_r} - 1} \frac{T}{\tau_v}\right) - \sqrt{\frac{2\sqrt{\gamma_r} + 1}{2\sqrt{\gamma_r} - 1}} \sin\left(\frac{1}{2}\sqrt{2\sqrt{\gamma_r} - 1} \frac{T}{\tau_v}\right) \right) \Theta(T) \end{aligned} \quad (57)$$

The optimal kernel, $M_r(T)$, is plotted in Fig. S4 for varying values of γ_r .

As the SNR γ_r increases, the initial response time and the adaptation time both get shorter. Although the kernel oscillates, its decay rate is faster than the period of oscillations. The time scales of decay and oscillation are closest to each other, and thus the oscillation amplitude is largest, when γ_r is large: in the limit that $\gamma_r \rightarrow \infty$, $\text{Re}[z_{r,2}] = \text{Im}[z_{r,2}] = \gamma_r^{1/4}$. Even in this limit, the peak of the kernel following the first

negative lobe occurs at time $T = 3\pi \gamma_r^{-1/4}$ and is smaller than the kernel's maximum value ($M_r(T = 0)$) by a factor of $e^{-3\pi/2} \sim 0.009$. Thus, the oscillations are small. $M_r(T)$ transitions continuously between the forms above as γ_r varies.

The results of this and previous section could also be derived using the continuous-time Kalman-Bucy filter (20,21). That approach provides a pair of ODEs for the estimator of s (i.e. conditional mean $\mu_{s|r}$) and its uncertainty (i.e. the conditional variance $\sigma_{s|r}^2$) that are driven by the observations, $r(t)$. Once $\sigma_{s|r}^2$ reaches steady state in that formulation (consistent with our assumption of stationarity here), the ODE for $\mu_{s|r}$ can be solved in terms of a kernel convolved with past $r(t)$, which is identical to the optimal kernel above.

Modeling kinase activity

In shallow gradients, CheA kinases respond approximately linearly to recent signals. We model kinase responses, $a(t)$, to past particle arrival rates, $r(t)$, in background particle arrival rate r_0 , as:

$$a(t) = a_0 - \int_{-\infty}^t K_r(t-t') (r(t') - r_0) dt' + \eta(t). \quad (58)$$

The response function to particle arrival rate, $K_r(T)$, is:

$$K_r(t) = G_r \left(\left(\frac{1}{\tau_1} + \frac{1}{\tau_2} \right) \exp\left(-\left(\frac{1}{\tau_1} + \frac{1}{\tau_2}\right)t\right) - \frac{1}{\tau_2} \exp\left(-\frac{t}{\tau_2}\right) \right) \Theta(t), \quad (59)$$

We note that in our previous work (3) we modeled kinase responses to signals, $s(t)$, directly. In the Methods section of the main text, we show how to convert between these representations (Equation 15 in the Methods).

The Fourier transform of this kernel is:

$$K_r(\omega) = \frac{G_r}{\tau_1} \frac{(-i\omega)}{\left(\frac{1}{\tau_2} - i\omega\right)\left(\frac{1}{\tau_1} + \frac{1}{\tau_2} - i\omega\right)}. \quad (60)$$

Particle arrival noise filtered through this kernel has spectrum:

$$N_r(\omega) = r_0 |K_r(\omega)|^2. \quad (61)$$

In experiments, we measure responses to absolute changes in concentration $c(t)$, with response kernel $K_c(T)$, which has the same form as $K_r(T)$ above, but with gain G_c . Then, we convert G_c to G_r via $G_r = G_c/k_D$, and thus convert $K_c(T)$ to $K_r(T)$. With this, the intensity of filtered particle noise in Eqn. 61 is proportional to $G_r^2 r_0 = G_c^2 c_0/k_D$. This conversion implies that *E. coli* respond to every particle arriving at their surface, which is unlikely. Instead, one might use an effective $k_D^{eff} < k_D$ to do the conversion above, which would increase our estimate for the intensity of filtered particle noise, being proportional to $G_c^2 c_0/k_D^{eff}$. However, modeling the filtered particle noise with $k_D^{eff} = k_D$ maximizes our estimate of *E. coli*'s information rate. Since we find that *E. coli* are far from the physical limit, this is a conservative modeling choice.

Next, we consider modeling noise in kinase activity. As explained in Fig. S3 above, the FRET system we use for measuring kinase activity has limited time resolution, about 0.3 s. This allows us to constrain slow fluctuations in kinase activity, whose correlation function is characterized by a single decaying exponential function (3,22):

$$\langle \eta(t)\eta(t') \rangle = N_n(t - t') = \sigma_n^2 \exp\left(-\frac{|t - t'|}{\tau_n}\right) = D_n \tau_n \exp\left(-\frac{|t - t'|}{\tau_n}\right). \quad (62)$$

The parameters here are the long-time variance σ_n^2 and the correlation time τ_n , which are related to the diffusivity of the noise by $D_n = \sigma_n^2/\tau_n$. The power spectrum of this noise is

$$N_n(\omega) = \frac{2 D_n}{\frac{1}{\tau_n^2} + \omega^2}. \quad (63)$$

There can also be noise at higher frequencies that we don't observe. Kinase responses to particle arrival noise set a minimum noise level at all frequencies. At high frequencies, simply extrapolating the power spectrum in Eqn. 63 drops below the implied filtered particle noise in Eqn. 61 if we take that τ_1 in Eqn. 59 to be the value measured previously in biochemical studies (1,2), $\tau_1 \approx 1/60$ s. One possibility is that cooperativity of the receptor-kinase lattice slows down τ_1 to a value closer to what we measure in FRET, $\tau_1 \approx 0.35$ s. In this case, extrapolating the slow noise to high frequencies does not cause any problems.

To avoid having unphysical noise power at high frequencies, we take the total noise in kinase activity to be a sum of the measured slow noise in Eqn. 63 plus the filtered particle arrival noise in Eqn. 61. There are likely other noise sources at high frequencies, so this modeling choice maximizes our estimate of *E. coli*'s information rate. Since we find that *E. coli* are far from the physical limit, this is a conservative modeling choice. Ultimately, even if we only model noise in kinase activity as being the slow, measurable noise, the effects on the numerical values of the information rate are small.

Before continuing, we will make an additional simplifying assumption. The adaptation time of kinase responses, τ_2 , and the correlation time of kinase noise, τ_n , are each roughly ~ 10 s. Therefore, below we will also assume $\tau_2 \approx \tau_n$, which also has small quantitative effects on the results. These simplifications also allow us to derive interpretable analytical expressions.

Derivation of the behaviorally-relevant information rate in kinase activity

In this section, we derive the information about current signal encoded in the kinase activity of a typical *E. coli* cell. Here, we seek an expression for the following transfer entropy rate:

$$\begin{aligned} I_{s \rightarrow a}^* &= \lim_{dt \rightarrow 0} \frac{1}{dt} I(a(t + dt); s(t) | \{a(t)\}) \\ &= -[\partial_\tau I(\{a(t)\}; s(t + \tau))]_{\tau=0}. \end{aligned} \quad (64)$$

Again, the calculation centers on calculating the mutual information between past kinase activity a and signal at some time τ into the future, $I(\{a(t)\}; s(t + \tau))$. The quantity we need to derive this is the posterior distribution of signal given past kinase activity, $P(s(t + \tau) | \{a(t)\})$. Past measurements by us

and others (3,22,23) have shown that kinase activity in wild type cells (i.e. cells with all receptor types and with their adaptation system intact) is well-approximated by a Gaussian process. Because of this, and because we consider shallow gradients, we only need the variance of $P(s(t + \tau)|\{a(t)\})$ to compute the mutual information to leading order in g (see the section **Derivation of the behaviorally-relevant information rate in particle arrivals**, above). Thus, we can approximate s and a as jointly Gaussian distributed.

With the approximation that s and a are also jointly Gaussian distributed, $P(s(t + \tau)|\{a(t)\})$ is Gaussian, and therefore we again need to compute a mean $\mu_{s|a}(\tau)$ and a variance $\sigma_{s|a}^2(\tau)$. Then, the mutual information can then be computed from:

$$I(\{a(t)\}; s(t + \tau)) = \frac{1}{2} \log \left(\frac{\sigma_s^2}{\sigma_{s|a}^2(\tau)} \right) = -\frac{1}{2} \log(1 - \rho_{as}^2(\tau)), \quad (65)$$

and the predictive information rate is

$$i_{s \rightarrow a}^* = \frac{1}{2} \left[\frac{-\partial_\tau \rho_{as}^2(\tau)}{1 - \rho_{as}^2(\tau)} \right]_{\tau=0} \quad (66)$$

Here, $\rho_{as}^2(\tau) = 1 - \frac{\sigma_{s|a}^2(\tau)}{\sigma_s^2}$ is the generalized correlation between $s(t + \tau)$ and past a , or the fraction reduction of variance in $s(t + \tau)$ upon observing past a .

To compute the rate of information transfer from current signal $s(t)$ to kinase activity $a(t)$, we need the conditional mean and variance of $s(t + \tau)$, $\mu_{s|a}(\tau)$ and $\sigma_{s|a}^2(\tau)$. These in turn require deriving the kernel $M_a(T)$ that maps past kinase activity a to the conditional mean, $\mu_{s|a}(\tau)$. This can again be derived using Wiener filtering theory and expressed in terms of the power spectra of s and a . These are:

$$S_s(\omega) = F[C_s(T)] = \frac{2 g^2 \frac{\sigma_v^2}{\tau_v}}{\frac{1}{\tau_v^2} + \omega^2} \quad (67)$$

$$S_a(\omega) = F[C_a(T)] = |K_r(\omega)|^2 S_r(\omega) + N_{n(\omega)} \quad (68)$$

$$= |K_r(\omega)|^2 \left(r_0^2 \frac{S_s(\omega)}{\omega^2} + r_0 \right) + \frac{2 D_n}{\frac{1}{\tau_2^2} + \omega^2} \quad (69)$$

$$= \left(\frac{G_r}{\tau_1} \right)^2 \frac{\omega^2}{\left(\frac{1}{\tau_2^2} + \omega^2 \right) \left(\left(\frac{1}{\tau_1} + \frac{1}{\tau_2} \right)^2 + \omega^2 \right)} \left(r_0^2 \frac{S_s(\omega)}{\omega^2} + r_0 \right) + \frac{2 D_n}{\frac{1}{\tau_2^2} + \omega^2} \quad (70)$$

$$S_{as}(\omega) = S_{sa}^*(\omega) = F[C_{as}(T)] = -K_r^*(\omega) S_{rs}(\omega) \quad (71)$$

$$= -\frac{G_r}{\tau_1} \frac{r_0}{\left(\frac{1}{\tau_2} + i\omega\right)\left(\frac{1}{\tau_1} + \frac{1}{\tau_2} + i\omega\right)} S_s(\omega) \quad (72)$$

where $C_s(T) = \langle s(t) s(t+T) \rangle$, $C_a(T) = \langle (a(t) - a_0)(a(t+T) - a_0) \rangle$, and $C_{as}(T) = \langle (a(t) - a_0) s(t+T) \rangle$. The first term in $S_a(\omega)$ comes from responses to signals, the second term comes from filtered particle arrival noise, and the third term comes from internal kinase noise. For convenience, we will define $\tau_3^{-1} = \tau_1^{-1} + \tau_2^{-1}$.

We now need to decompose $S_a(\omega)$ into the product of a causal and an anti-causal part by finding its zeros and poles. The zeros satisfy $S_a(\omega = i z_a) = 0$ are complex solutions to the equation:

$$\frac{G_r^2}{\tau_1^2} \left(2 r_0^2 g^2 \frac{\sigma_v^2}{\tau_v} + r_0 \omega^2 \left(\frac{1}{\tau_v^2} + \omega^2 \right) \right) + 2 D_n \left(\frac{1}{\tau_v^2} + \omega^2 \right) \left(\frac{1}{\tau_3^2} + \omega^2 \right) = 0. \quad (73)$$

This can be written in terms of the particle arrival SNR, $\gamma_r = 2 r_0 g^2 \sigma_v^2 \tau_v^3$, and the ratio of the diffusivity of filtered particle noise and the diffusivity of slow kinase noise, $R = \frac{1}{2} \frac{G_r^2}{\tau_1^2} \frac{r_0}{D_n}$:

$$R \left(\gamma_r + \tau_v^2 \omega^2 (1 + \tau_v^2 \omega^2) \right) + (1 + \tau_v^2 \omega^2) \left(\frac{\tau_v^2}{\tau_3^2} + \tau_v^2 \omega^2 \right) = 0 \quad (74)$$

The zeros of $S_a(\omega)$ are:

$$\begin{aligned} i z_{a,1} &= i \frac{1}{\tau_v} \frac{1}{\sqrt{2(1+R)}} \sqrt{\left(\frac{\tau_v}{\tau_3}\right)^2 + (1+R) - \sqrt{(1+R)(1+R(1-4\gamma_r)) - 2(1+R)\left(\frac{\tau_v}{\tau_3}\right)^2 + \left(\frac{\tau_v}{\tau_3}\right)^4}}, \\ i z_{a,2} &= i \frac{1}{\tau_v} \frac{1}{\sqrt{2(1+R)}} \sqrt{\left(\frac{\tau_v}{\tau_3}\right)^2 + (1+R) + \sqrt{(1+R)(1+R(1-4\gamma_r)) - 2(1+R)\left(\frac{\tau_v}{\tau_3}\right)^2 + \left(\frac{\tau_v}{\tau_3}\right)^4}} \end{aligned} \quad (75)$$

as well as their complex conjugates.

The poles of $S_a(\omega)$ satisfy $\frac{1}{S_a(\omega=i p_a)} = 0$ and are $i p_{a,1} = i \frac{1}{\tau_v}$, $i p_{a,2} = i \frac{1}{\tau_2}$, and $i p_{a,3} = i \frac{1}{\tau_3}$, as well as their complex conjugates.

We decompose $S_a(\omega)$ as:

$$S_a(\omega) = \phi_a(\omega) \phi_a^*(\omega) \quad (76)$$

where

$$\phi_a(\omega) = \sqrt{2 D_n (1+R)} \frac{(z_{a,1} - i\omega)(z_{a,2} - i\omega)}{(p_{a,1} - i\omega)(p_{a,2} - i\omega)(p_{a,3} - i\omega)}. \quad (77)$$

Next, we need the causal part of the following (see Appendix A):

$$\frac{S_{as}(\omega)}{\phi_a^*(\omega)} e^{-i\omega\tau} = -\frac{G_r/\tau_1}{\sqrt{2D_n(1+R)}} \frac{2r_0 g^2 \sigma_v^2 \frac{1}{\tau_v}}{\left(\frac{1}{\tau_v} - i\omega\right) (z_{a,1} + i\omega) (z_{a,2} + i\omega)} e^{-i\omega\tau} \quad (78)$$

Again, we find the causal part of this expression by doing a partial fraction decomposition and keeping only the terms with poles and zeros that have negative imaginary part:

$$\frac{S_{as}(\omega)}{\phi_a^*(\omega)} e^{-i\omega\tau} = \frac{A}{\left(\frac{1}{\tau_v} - i\omega\right)} + \frac{B}{(z_{a,1} + i\omega)} + \frac{C}{(z_{a,2} + i\omega)}, \quad (79)$$

for unknown A , B , and C . Only the pole of the first term (at $\omega = -i\frac{1}{\tau_v}$) has negative imaginary part, so we only need to compute A to get the causal part of this expression. This is:

$$A = \left[-\frac{G_r/\tau_1}{\sqrt{2D_n(1+R)}} \frac{2r_0 g^2 \sigma_v^2 \frac{1}{\tau_v}}{(z_{a,1} + i\omega) (z_{a,2} + i\omega)} e^{-i\omega\tau} \right]_{\omega = -i\frac{1}{\tau_v}} \quad (80)$$

$$= -\frac{G_r/\tau_1}{\sqrt{2D_n(1+R)}} \frac{2r_0 g^2 \sigma_v^2 \tau_v}{(1 + z_{a,1} \tau_v)(1 + z_{a,2} \tau_v)} e^{-\frac{\tau}{\tau_v}}, \quad (81)$$

and the causal part of $S_{as}(\omega)/\phi_a^*(\omega)$ is then:

$$\left[\frac{S_{as}(\omega)}{\phi_a^*(\omega)} e^{-i\omega\tau} \right]^+ = -\frac{G_r/\tau_1}{\sqrt{2D_n(1+R)}} \frac{2r_0 g^2 \sigma_v^2 \tau_v}{(1 + z_{a,1} \tau_v)(1 + z_{a,2} \tau_v)} \frac{e^{-\frac{\tau}{\tau_v}}}{\left(\frac{1}{\tau_v} - i\omega\right)}. \quad (82)$$

Finally, like $C_{rs}(\tau)$ in the section above, $C_{as}(\tau) \propto \exp\left(-\frac{\tau}{\tau_v}\right)$ when $\tau \geq 0$.

With these expressions, the optimal kernel that computes the mean of $p(s(t+\tau)|\{a\})$ is (Appendix A):

$$M_a(\omega) = \frac{1}{\phi_a(\omega)} \left[\frac{S_{as}(\omega)}{\phi_a^*(\omega)} e^{-i\omega\tau} \right]^+ \quad (83)$$

$$= -e^{-\frac{\tau}{\tau_v}} \frac{2\frac{G_r}{\tau_1} r_0 g^2 \sigma_v^2 \tau_v}{2D_n(1+R)(1+z_{a,1}\tau_v)(1+z_{a,2}\tau_v)} \frac{\left(\frac{1}{\tau_2} - i\omega\right) \left(\frac{1}{\tau_3} - i\omega\right)}{(z_{a,1} - i\omega)(z_{a,2} - i\omega)} \quad (84)$$

We discuss this kernel in the following section.

The variance of $P(s(t+\tau)|\{a\})$, $\sigma_{s|a}^2(\tau)$, is (Appendix A, Eqn. 127):

$$\sigma_{s|a}^2(\tau) = \sigma_s^2 - \frac{1}{2\pi} \int_{-\infty}^{\infty} S_{as}^*(\omega) e^{i\omega\tau} M_a(\omega) d\omega \quad (85)$$

$$= \sigma_s^2 \left(1 - e^{-2\frac{\tau}{\tau_v}} \frac{2 \frac{G_r^2}{\tau_1^2} r_0^2 g^2 \sigma_v^2 \tau_v^3}{2 D_n (1+R)(1+z_{a,1} \tau_v)^2 (1+z_{a,2} \tau_v)^2} \right), \quad (86)$$

where $\sigma_s^2 = g^2 \sigma_v^2$. Therefore, the correlation coefficient $\rho_{as}^2(\tau)$ is:

$$\rho_{as}^2(\tau) = 1 - \frac{\sigma_{s|a}^2(\tau)}{\sigma_s^2} = e^{-2\frac{\tau}{\tau_v}} \frac{2 \frac{G_r^2}{\tau_1^2} r_0^2 g^2 \sigma_v^2 \tau_v^3}{2 D_n (1+R)(1+z_{a,1} \tau_v)^2 (1+z_{a,2} \tau_v)^2}, \quad (87)$$

or in terms of $\gamma_r = 2 r_0 g^2 \sigma_v^2 \tau_v^3$ and $R = \frac{1}{2} \frac{G_r^2 r_0}{\tau_1^2 D_n}$:

$$= e^{-2\frac{\tau}{\tau_v}} \frac{R}{(1+R)} \frac{\gamma_r}{(1+z_{a,1} \tau_v)^2 (1+z_{a,2} \tau_v)^2}. \quad (88)$$

Finally, using Eqn. 66 above, we find that the information about current signal encoded in *E. coli*'s kinase activity is:

$$\dot{I}_{s \rightarrow a}^* = \frac{1}{\tau_v} \frac{\rho_{as}^2(\tau=0)}{1 - \rho_{as}^2(\tau=0)} = \frac{1}{\tau_v} \frac{\frac{R}{(1+R)} \frac{\gamma_r}{(1+z_{a,1} \tau_v)^2 (1+z_{a,2} \tau_v)^2}}{1 - \frac{R}{(1+R)} \frac{\gamma_r}{(1+z_{a,1} \tau_v)^2 (1+z_{a,2} \tau_v)^2}}. \quad (89)$$

In shallow gradients, $\dot{I}_{s \rightarrow a}^* \approx \frac{1}{\tau_v} \rho_{as}^2(\tau=0) \approx \frac{2}{\tau_v} I(\{a(t); s(t)\})$, and only the leading order g^2 term of $\dot{I}_{s \rightarrow a}^*$ contributes to the final expression. Since $\gamma_r \propto g^2$ in Eqn. 88, we can get the shallow-gradient expression for $\dot{I}_{s \rightarrow a}^*$ by evaluating $z_{a,1}$ and $z_{a,2}$ at $g = 0$. This is equivalent to taking $\gamma_r \rightarrow 0$, which gives:

$$z_{a,1} \approx \frac{1}{\tau_3 \sqrt{1+R}}, \quad z_{a,2} \approx \frac{1}{\tau_v}. \quad (90)$$

Thus, in shallow gradients, we get:

$$\dot{I}_{s \rightarrow a}^* \approx \frac{1}{\tau_v} \frac{1}{4} \frac{R}{1+R} \frac{\gamma_r}{\left(1 + \frac{\tau_v}{\tau_3} \frac{1}{\sqrt{1+R}}\right)^2} = \frac{1}{\tau_v} \frac{1}{4} \frac{\frac{1}{2} \frac{G_r^2 r_0}{\tau_1^2 D_n}}{1 + \frac{1}{2} \frac{G_r^2 r_0}{\tau_1^2 D_n}} \frac{2 r_0 g^2 \sigma_v^2 \tau_v^3}{\left(1 + \frac{\tau_v}{\tau_3} \left(1 + \frac{1}{2} \frac{G_r^2 r_0}{\tau_1^2 D_n}\right)^{-1/2}\right)^2}, \quad (91)$$

where again $\tau_3^{-1} = \tau_1^{-1} + \tau_2^{-1}$. Furthermore, since $\tau_1 \ll \tau_v$, taking $\tau_1 \rightarrow 0$ only slightly increases the information rate and gives a simpler expression in terms of a kinase signal to noise ratio, $\gamma_a = \frac{G_r^2}{D_n} r_0^2 g^2 \sigma_v^2 \tau_v$, and the particle arrival signal to noise ratio, $\gamma_r = 2 r_0 g^2 \sigma_v^2 \tau_v^3$:

$$I_{s \rightarrow a}^* \approx \frac{1}{\tau_v} \frac{1}{4} \gamma_a \frac{\frac{\gamma_r}{\gamma_a}}{\left(1 + \sqrt{\frac{\gamma_r}{\gamma_a}}\right)^2} = \frac{1}{\tau_v} \frac{1}{4} \frac{G_r^2}{D_n} r_0^2 g^2 \sigma_v^2 \tau_v \frac{\frac{2 D_n \tau_v^2}{G_r^2 r_0}}{\left(1 + \sqrt{\frac{2 D_n \tau_v^2}{G_r^2 r_0}}\right)^2}. \quad (92)$$

We also note that for finite g but $\tau_1 \rightarrow 0$, $z_{a,1}$ and $z_{a,2}$ are:

$$z_{a,1} \approx \frac{1}{\tau_v} \frac{1}{\sqrt{2}} \sqrt{1 + \frac{\gamma_r}{\gamma_a} - \sqrt{1 - 4 \gamma_r - 2 \frac{\gamma_r}{\gamma_a} + \left(\frac{\gamma_r}{\gamma_a}\right)^2}},$$

$$z_{a,2} \approx \frac{1}{\tau_v} \frac{1}{\sqrt{2}} \sqrt{1 + \frac{\gamma_r}{\gamma_a} + \sqrt{1 - 4 \gamma_r - 2 \frac{\gamma_r}{\gamma_a} + \left(\frac{\gamma_r}{\gamma_a}\right)^2}}. \quad (93)$$

We plugged these expressions into Eqn. 89, with $\frac{R}{1+R} \rightarrow 1$ as $\tau_1 \rightarrow 0$, to generate the plots in Fig. 3 of the main text.

Eqns. 44, 52, and 89 for the information rates $I_{s \rightarrow r}^*$ and $I_{s \rightarrow a}^*$ are nearly exact, but make several assumptions. They require $r_0 \tau_v \gg 1$ so that we can approximate particle arrivals as Gaussian. They also use Gaussian approximations for the mutual information quantities $I(s(t); \{r\})$ and $I(s(t); \{a\})$, which are valid when these quantities are small (shallow gradients, small g). We used linear theory to model kinase responses, which is valid if deviations in kinase activity from baseline are small—i.e. when g is small. And we ignored feedbacks in which responses to signals change the signal statistics that the cell experiences, again valid when g is small. Each of these assumptions can break at a different characteristic value of g : for particle arrival rate, small g means $\gamma_r \ll 1$; for kinase activity, small g means $\gamma_a \ll 1$. That all said, Eqns. 44, 52, and 89 currently provide our best analytical insight into information transfer during chemotaxis.

Optimal kernel for estimating signal from kinase activity

To understand the kernel $M_a(\omega)$ that constructs an estimate of the current signal, $s(t)$, from past kinase activity, $\{a\}$, we first multiply it by the kinase response function of particle arrivals, $K_r(\omega)$. This gives a composite kernel that effectively maps the past of particle arrivals r , corrupted by kinase noise, to an estimate of the signal $s(t)$:

$$-M_a(\omega) K_r(\omega) = - \frac{2 \left(\frac{G_r}{\tau_1}\right)^2 r_0 g^2 \sigma_v^2 \tau_v}{2 D_n (1+R) (1+z_{a,1} \tau_v)(1+z_{a,2} \tau_v)} \frac{(-i \omega)}{(z_{a,1} - i \omega)(z_{a,2} - i \omega)}. \quad (94)$$

In the time domain, this is:

$$IFT[-M_a(\omega) K_r(\omega)] = \frac{2 \left(\frac{G_r}{\tau_1}\right)^2 r_0 g^2 \sigma_v^2 \tau_v}{2 D_n (1+R)} \frac{(z_{a,2} \exp(-z_{a,2} t) - z_{a,1} \exp(-z_{a,1} t))}{(1+z_{a,1} \tau_v)(1+z_{a,2} \tau_v)(z_{a,1} - z_{a,2})} \Theta(t). \quad (95)$$

This composite kernel that effectively acts on particle arrivals has the same structure as the optimal kernel $M_r(T)$ (Eqn. 53) for directly constructing $s(t)$ from particle arrivals. It's biphasic and adapts perfectly, although with different time scales than $M_r(T)$. This means that $M_a(T)$ attempts to invert the kinase response function $K_r(T)$, to the extent possible given the kinase noise $N_n(T)$, and then apply something as close as possible to the optimal kernel for particle counts, $M_r(T)$.

Taking this line of thinking further, the optimal kernel acting on particle counts, $M_r(T)$, is the kernel that the cell should *try* to implement (up to changes of units). However, the cell has to communicate information about the signal $s(t)$ through multiple chemical species in order to send them from the kinases at one location to the motors at various other locations. These steps impose constraints on the cell's signaling pathway, and they add noise. Despite this, the cell should be attempting to make its composite kernel from input (particle counts) to output (tumble rate) look like $M_r(T)$.

Information about current versus past signals encoded in kinase activity

We previously quantified the information about all past signals encoded in kinase activity, $\dot{I}_{s \rightarrow a}$, and found that *E. coli* use this information efficiently: they climb gradients at speeds near the information-performance limit (3). There are two possible inefficiencies that prevent *E. coli* from reaching the limit: first, cells might encode information about past signals, which don't contribute to gradient-climbing; and second, information about current signal can be lost in communication to the motor behavior. Now that we have an expression for the information about current signal $s(t)$ in kinase activity, we can distinguish between these two effects.

We defined the information about all past signals encoded in kinase activity using the following transfer entropy rate:

$$\dot{I}_{s \rightarrow a} \equiv \lim_{dt \rightarrow 0} \frac{1}{dt} I(a(t+dt); \{s\} | \{a\}). \quad (96)$$

The subset of this information that is relevant to chemotaxis is:

$$\dot{I}_{s \rightarrow a}^* \equiv \lim_{dt \rightarrow 0} \frac{1}{dt} I(a(t+dt); s(t) | \{a\}), \quad (97)$$

which is the information we have considered here. How do these information rates compare to each other for the kinase response function and noise correlation function that we measured here and previously?

First, note that if kinase activity a were Markovian in $s(t)$, then we would have

$$\begin{aligned} \dot{I}_{s \rightarrow a} &= \lim_{dt \rightarrow 0} \frac{1}{dt} I(a(t+dt); \{s\} | \{a\}) \\ &= \lim_{dt \rightarrow 0} \frac{1}{dt} I(a(t+dt); s(t) | \{a\}) \\ &= \dot{I}_{s \rightarrow a}^* \end{aligned} \quad (98)$$

and all information about signals encoded in kinase activity is relevant to gradient climbing. Surprisingly, this means that a long response adaptation time does not necessarily degrade information about the current signal.

We can evaluate both of these information rates for the response and noise models used here. In the regime of shallow gradients and $\tau_2 \approx \tau_n$, the information about past and present signals is (3,25):

$$\dot{I}_{s \rightarrow a} \approx \frac{1}{4\pi} \int_{-\infty}^{\infty} \frac{S(\omega) \frac{r_0^2}{\omega^2} |K_r(\omega)|^2}{N_n(\omega) + r_0 |K_r(\omega)|^2} d\omega \quad (99)$$

$$= \frac{\frac{G_r^2}{\tau_1^2} r_0^2 g^2 \sigma_v^2 \tau_3^2}{4 D_n \left(1 + \frac{\tau_3}{\tau_v} \sqrt{1 + \frac{G_r^2}{\tau_1^2} \frac{r_0}{2 D_n}} \right)} = \frac{1}{\tau_v} \frac{1}{4} \frac{R \gamma_r \left(\frac{\tau_3}{\tau_v} \right)^2}{\left(1 + \frac{\tau_3}{\tau_v} \sqrt{1 + R} \right)} \quad (100)$$

which we have expressed in terms of the ratio of the diffusivity of filtered particle noise and the diffusivity of slow kinase noise, $R = \frac{G_r^2}{\tau_1^2} \frac{r_0}{2 D_n}$; the particle arrival signal-to-noise ratio, $\gamma_r = 2 r_0 g^2 \sigma_v^2 \tau_3^3$; and $\tau_3^{-1} = \tau_1^{-1} + \tau_2^{-1}$.

We compare this to the information about current signal only derived in the previous section, Eqn. 91, reproduced below:

$$\dot{I}_{s \rightarrow a}^* = \frac{1}{\tau_v} \frac{1}{4} \frac{R}{1 + R} \frac{\gamma_r}{\left(1 + \frac{\tau_v}{\tau_3} \frac{1}{\sqrt{1 + R}} \right)^2} \quad (101)$$

The ratio of these two information rates has a particularly simple form:

$$\frac{\dot{I}_{s \rightarrow a}^*}{\dot{I}_{s \rightarrow a}} \approx \frac{\tau_v}{\tau_3 \sqrt{1 + R} + \tau_v} = \frac{\tau_v}{\tau_3 \sqrt{1 + \frac{G_r^2}{\tau_1^2} \frac{r_0}{2 D_n}} + \tau_v}. \quad (102)$$

Thus, for $\dot{I}_{s \rightarrow a}$ to mostly carry information about current signal and be close to $\dot{I}_{s \rightarrow a}^*$, 1) the time scale of initial kinase response must be short compared to the signal correlation time, $\tau_1 \ll \tau_v$; and 2) the diffusivity of filtered particle noise must be small compared to that of internal kinase noise, $G_r^2 r_0 \ll 2 D_n$. Using $\tau_1 = 1/60$ s from biochemistry studies Refs. (1,2), we estimate that $\frac{\dot{I}_{s \rightarrow a}^*}{\dot{I}_{s \rightarrow a}} \approx 0.88 \pm 0.01$ in $c_0 = 1 \mu\text{M}$, and increases as c_0 gets large or small. This suggests that *E. coli*'s main source of "inefficiency" is that relevant information in kinase activity is lost in communication with the motors.

This result might appear to be in contradiction with the results of Ref. (16), which found that the fraction of predictive information about signals relative to past information about signals was very small (about 1%) in a model of *E. coli*'s kinase activity, a , and downstream readout molecules, x (CheYp). (Our $\dot{I}_{s \rightarrow a}^*$, being a predictive information rate, is very similar to their predictive information, while $\dot{I}_{s \rightarrow a}$ is very similar to their past information.) However, that study considered predictive and past information encoded in

the *current* value of the readout molecule, $x(t)$, instead of the entire history of readout molecules $\{x\}$. This difference in how our information quantities are defined explains the large difference.

Kinase activity a and even CheY phosphorylation level downstream x are not the final outputs of the chemotaxis system. Instead, downstream pathway dynamics can act on the entire past of a or x to extract more information and make behavioral decisions. Therefore, the current values of $a(t)$ and $x(t)$ do not need to be faithful estimates of the current (or future) signal $s(t)$; they just need to carry decodable information about $s(t)$ in their trajectories. Our information measures above account for this.

In summary, we have two sets of inequalities. The first set of inequalities,

$$\dot{I}_{s \rightarrow a} \geq \dot{I}_{s \rightarrow a}^* \geq \dot{I}_{s \rightarrow m}^* \propto \left(\frac{v_d}{v_0}\right)^2, \quad (103)$$

was the focus of our previous work (3), and it quantifies how efficiently *E. coli* use the information *that they have* at the level of kinase activity, $\dot{I}_{s \rightarrow a}$, to climb gradients. The main result of that work was that $\dot{I}_{s \rightarrow a} \approx 2 \dot{I}_{s \rightarrow m}^*$. The analysis above adds to this: $\dot{I}_{s \rightarrow a} \approx \dot{I}_{s \rightarrow a}^* \approx 2 \dot{I}_{s \rightarrow m}^*$.

The second set of inequalities,

$$\dot{I}_{s \rightarrow r}^* \geq \dot{I}_{s \rightarrow a}^* \geq \dot{I}_{s \rightarrow m}^* \propto \left(\frac{v_d}{v_0}\right)^2, \quad (104)$$

particularly the left-most one, is the focus of this work. It quantifies how much information *E. coli* get compared to the physical limit. The main result of this manuscript is that $\dot{I}_{s \rightarrow r}^* \gg \dot{I}_{s \rightarrow a}^*$.

Appendix A: Causal Wiener filter derivation

Causal Wiener filtering theory seeks a linear estimator of an unknown quantity $s(t + \tau)$ at time τ in the future, from past observations of a quantity x that is correlated with s (26). The past of x is denoted $\{x(t)\}$. Both s and x are assumed to be stationary stochastic processes with zero means: $\langle x(t) \rangle = \langle s(t) \rangle = 0$. The Wiener filter, $M_x(T)$, is the kernel that minimizes the mean squared error of the estimator:

$$M_x(T) = \operatorname{argmin}_{K(T)} \langle e^2(\tau) \rangle = \operatorname{argmin}_{K(T)} \left\langle \left(s(t + \tau) - \int_{-\infty}^t K(t - t') x(t') dt' \right)^2 \right\rangle. \quad (105)$$

In general, the estimator of $s(t + \tau)$ that minimizes the mean squared error is the conditional mean $\langle s(t + \tau) | \{x(t)\} \rangle$. In the case of Gaussian-distributed s and x , the conditional mean $\langle s(t + \tau) | \{x(t)\} \rangle$ is exactly a linear function of $\{x(t)\}$, so the linear estimator above is the global optimum. The minimum error $\langle e^*(\tau)^2 \rangle = \sigma_{s|x}^2(\tau)$ is the conditional variance of $s(t + \tau)$ given past x . The main technical challenge of finding the optimal kernel is the constraint that it must be causal: $M_x(T) = 0$ for $T < 0$.

To derive the optimal kernel, first we expand the square in the objective function:

$$\langle e^2(\tau) \rangle = \left\langle s(t + \tau)^2 - 2 s(t + \tau) \int_{-\infty}^{\infty} K(t - t') x(t') dt' + \int_{-\infty}^{\infty} K(t - t') x(t') dt' \int_{-\infty}^{\infty} K(t - t'') x(t'') dt'' \right\rangle, \quad (106)$$

and move the expectation inside of the integrals:

$$= \sigma_s^2 - 2 \int_{-\infty}^{\infty} K(t-t') \langle s(t+\tau) x(t') \rangle dt' + \int_{-\infty}^{\infty} \int_{-\infty}^{\infty} K(t-t') K(t-t'') \langle x(t') x(t'') \rangle dt' dt'' . \quad (107)$$

Here we used time-translation invariance of s : $\langle s(t+\tau)^2 \rangle = \langle s(t)^2 \rangle = \sigma_s^2$. Next, change variables to $t' \rightarrow \tau' = t - t'$ and $t'' \rightarrow \tau'' = t - t''$, replacing absolute time with time delays. τ' and $\tau'' > 0$ correspond to time delay into the past.

$$= \sigma_s^2 - 2 \int_{-\infty}^{\infty} K(\tau') \langle s(t+\tau) x(t-\tau') \rangle d\tau' + \int_{-\infty}^{\infty} \int_{-\infty}^{\infty} K(\tau') K(\tau'') \langle x(t-\tau') x(t-\tau'') \rangle d\tau' d\tau'' . \quad (108)$$

Defining the cross-correlation function $C_{xs}(t-t') = \langle x(t') s(t) \rangle$ and autocorrelation function $C_x(t-t') = \langle x(t') x(t) \rangle$:

$$= \sigma_s^2 - 2 \int_{-\infty}^{\infty} K(\tau') C_{xs}(\tau' + \tau) d\tau' + \int_{-\infty}^{\infty} \int_{-\infty}^{\infty} K(\tau') K(\tau'') C_x(\tau'' - \tau') d\tau' d\tau'' . \quad (109)$$

When $\tau > 0$ in $C_{xy}(\tau)$, y is evaluated at a time point in the future relative to x . Note that $C_{sx}(\tau) = C_{xs}(-\tau)$.

Next, we take the functional derivative of the mean squared error with respect to $K(T)$:

$$\frac{\delta \langle e^2(\tau) \rangle}{\delta K} = -2 C_{xs}(\tau' + \tau) + \int_{-\infty}^{\infty} K(\tau'') C_x(\tau'' - \tau') d\tau'' + \int_{-\infty}^{\infty} K(\tau'') C_x(\tau' - \tau'') d\tau'' \quad (110)$$

Since $C_x(\tau) = C_x(-\tau)$, this is:

$$= -2 C_{xs}(\tau' + \tau) + 2 \int_{-\infty}^{\infty} K(\tau'') C_x(\tau'' - \tau') d\tau'' . \quad (111)$$

Now we need to consider the causal constraint on $K(T)$. For optimality with this constraint, the equation above must equal zero for $\tau' \geq 0$ (at times when x precedes s in C_{xs}). Otherwise, for $\tau' < 0$, the derivative is not necessarily zero. Therefore, at the optimum we can write (27):

$$\int_{-\infty}^{\infty} M_x(\tau'') C_x(\tau' - \tau'') d\tau'' - C_{xs}(\tau' + \tau) = A(\tau') \quad (112)$$

where

$$A(\tau') = \begin{cases} 0, & \tau' \geq 0 \\ a(\tau'), & \tau' < 0 \end{cases} \quad (113)$$

and $a(\tau')$ is some unspecified function. $A(\tau')$ is therefore anti-causal – it is only non-zero at times in the future ($\tau' < 0$). At first glance, this optimality condition might seem less constrained than if $A(\tau')$ were zero for all τ' (the optimality condition for the optimal non-causal filter). However, the fact that $A(\tau')$ is nonzero for $\tau' < 0$ actually limits the space of filters $M_x(\tau)$ that keep $A(\tau') = 0$ for $\tau' \geq 0$, as we will see below.

Next, we take the Fourier transform of both sides, defined as $f(\omega) = F[f(t)] = \int_{-\infty}^{\infty} f(t) e^{i\omega t} dt$.

Convolutions in the time domain become element-wise products in the Fourier domain:

$$M_x(\omega) C_x(\omega) = C_{xs}(\omega) e^{-i \omega \tau} + A(\omega). \quad (114)$$

On the left-hand side, we have the product of a causal function and a function that is nonzero for positive and negative time delays, the result of which is also nonzero for positive and negative time delays. On the right-hand side, we have a function that is nonzero for positive and negative time delays and an anti-causal function. How do we get the optimal causal kernel $M_x(\omega)$ out of this?

Naively, one might divide both sides by $C_x(\omega)$ and then multiply element-wise by a Heaviside step function in the time domain to get a causal kernel $M_x(\omega)$. However, although the resulting kernel is causal, it does not satisfy the optimality condition. Plugging that kernel back into Eqn. 114, it multiplies the non-causal $C_x(\omega)$, and the result is non-causal. Thus, $A(\omega)$ is non-causal, so that kernel does not satisfy the optimality condition, $A(\tau') = 0$ for $\tau' \geq 0$.

Instead, we need to split $C_x(\omega)$ into causal and anti-causal parts, called a spectral factorization or Wiener-Hopf factorization (17–19):

$$C_x(\omega) = \phi(\omega) \phi^*(\omega), \quad (115)$$

where $\phi(\omega)$ is a causal function in the time domain and its complex conjugate $\phi^*(\omega)$ is anti-causal. $\phi(\omega)$ is constructed by putting all poles and zeros of $C_x(\omega)$ with negative real part into $\phi(\omega)$ and those with positive real part into $\phi^*(\omega)$.

Plugging this into the optimality condition:

$$M_x(\omega) \phi(\omega) \phi^*(\omega) = C_{xs}(\omega) e^{-i \omega \tau} + A(\omega) \quad (116)$$

$$M_x(\omega) \phi(\omega) = \frac{C_{xs}(\omega)}{\phi^*(\omega)} e^{-i \omega \tau} + \frac{A(\omega)}{\phi^*(\omega)}. \quad (117)$$

The left-hand side is now a causal function in the time domain, being the product of causal functions, and the right-hand side contains a non-causal function and an anti-causal function.

Multiplying both sides of Eqn. 117 by a Heaviside function in the time domain and then transforming back to Fourier space eliminates the anti-causal term $\frac{A(\omega)}{\phi^*(\omega)}$ and leaves the left-hand side unaffected:

$$M_x(\omega) \phi(\omega) = \left[\frac{C_{xs}(\omega)}{\phi^*(\omega)} e^{-i \omega \tau} \right]^+. \quad (118)$$

Now the right-hand side is causal, and dividing by $\phi(\omega)$ gives the optimal causal filter:

$$M_x(\omega) = \frac{1}{\phi(\omega)} \left[\frac{C_{xs}(\omega)}{\phi^*(\omega)} e^{-i \omega \tau} \right]^+. \quad (119)$$

To check that this filter satisfies the optimality condition (Eqn. 114), we can plug it in:

$$\frac{1}{\phi(\omega)} \left[\frac{C_{xs}(\omega)}{\phi^*(\omega)} e^{-i \omega \tau} \right]^+ \phi(\omega) \phi^*(\omega) = C_{xs}(\omega) e^{-i \omega \tau} + A(\omega) \quad (120)$$

$$\left[\frac{C_{xs}(\omega)}{\phi^*(\omega)} e^{-i \omega \tau} \right]^+ \phi^*(\omega) = C_{xs}(\omega) e^{-i \omega \tau} + A(\omega) \quad (121)$$

$$\left[\frac{C_{xs}(\omega)}{\phi^*(\omega)} e^{-i\omega\tau} \right]^+ = \frac{C_{xs}(\omega)}{\phi^*(\omega)} e^{-i\omega\tau} + \frac{A(\omega)}{\phi^*(\omega)}. \quad (122)$$

Now the left-hand side is the causal part of the first term on the right-hand side. Therefore, their difference is anti-causal and $A(\omega)$ is thus anti-causal, as desired:

$$A(\omega) = -\phi^*(\omega) \left[\frac{C_{xs}(\omega)}{\phi^*(\omega)} e^{-i\omega\tau} \right]^-. \quad (123)$$

At the optimum, the mean square error $\langle e^2(\tau) \rangle = \sigma_{s|x}^2(\tau)$ is:

$$\sigma_{s|x}^2(\tau) = \sigma_s^2 - 2 \int_0^\infty M_x(\tau') C_{xs}(\tau' + \tau) d\tau' + \int_0^\infty \int_0^\infty M_x(\tau') M_x(\tau'') C_x(\tau'' - \tau') d\tau' d\tau'', \quad (124)$$

where we have set the lower limit to zero because the kernel $M_x(T)$ is zero for $T < 0$. Using the optimality condition $\int_0^\infty M_x(\tau'') C_x(\tau'' - \tau') d\tau'' - C_{xs}(\tau' + \tau) = 0$ for $\tau' \geq 0$, we get:

$$= \sigma_s^2 - \int_0^\infty M_x(\tau') C_{xs}(\tau' + \tau) d\tau'. \quad (125)$$

Since $C_{xs}(\tau) = C_{sx}(-\tau)$, this is:

$$= \sigma_s^2 - \int_{-\infty}^\infty M_x(\tau') C_{sx}(-\tau - \tau') d\tau', \quad (126)$$

which is the convolution of $M_x(T)$ and $C_{sx}(T)$, with the result evaluated at $-\tau$. This can be expressed using their Fourier transforms (note the minus sign in front of tau in equation (112) leads to a plus sign in the exponent below) as:

$$\sigma_{s|x}^2(\tau) = \sigma_s^2 - \frac{1}{2\pi} \int_{-\infty}^\infty M_x(\omega) C_{sx}(\omega) e^{i\omega\tau} d\omega. \quad (127)$$

Plugging in the optimal kernel:

$$= \sigma_s^2 - \frac{1}{2\pi} \int_{-\infty}^\infty \frac{C_{sx}(\omega)}{\phi(\omega)} \left[\frac{C_{xs}(\omega)}{\phi^*(\omega)} e^{-i\omega\tau} \right]^+ e^{i\omega\tau} d\omega. \quad (128)$$

Finally, the correlation coefficient is:

$$\rho_{xs}^2(\tau) = 1 - \frac{\sigma_{s|x}^2(\tau)}{\sigma_s^2} = \frac{1}{\sigma_s^2} \frac{1}{2\pi} \int_{-\infty}^\infty \frac{C_{sx}(\omega)}{\phi(\omega)} \left[\frac{C_{xs}(\omega)}{\phi^*(\omega)} e^{-i\omega\tau} \right]^+ e^{i\omega\tau} d\omega. \quad (129)$$

Supplemental References

1. Levit MN, Grebe TW, Stock JB. Organization of the Receptor-Kinase Signaling Array That Regulates Escherichia coli Chemotaxis. J Biol Chem. 2002 Sep 27;277(39):36748–54.

2. Francis NR, Levit MN, Shaikh TR, Melanson LA, Stock JB, DeRosier DJ. Subunit Organization in a Soluble Complex of Tar, CheW, and CheA by Electron Microscopy. *J Biol Chem*. 2002 Sep 27;277(39):36755–9.
3. Mattingly HH, Kamino K, Machta BB, Emonet T. *Escherichia coli* chemotaxis is information limited. *Nat Phys*. 2021 Dec;17(12):1426–31.
4. Cover TM, Thomas JA. *Elements of Information Theory*. New York, NY: Wiley-Interscience; 1991.
5. Sigtermans D. Towards a Framework for Observational Causality from Time Series: When Shannon Meets Turing. *Entropy*. 2020 Apr;22(4):426.
6. Bialek W, De Ruyter Van Steveninck RR, Tishby N. Efficient representation as a design principle for neural coding and computation. In: 2006 IEEE International Symposium on Information Theory. 2006. p. 659–63.
7. Palmer SE, Marre O, Berry MJ, Bialek W. Predictive information in a sensory population. *PNAS*. 2015 Jun 2;112(22):6908–13.
8. Becker NB, Mugler A, ten Wolde PR. Optimal Prediction by Cellular Signaling Networks. *Phys Rev Lett*. 2015 Dec 17;115(25):258103.
9. Cardoso JF. Dependence, Correlation and Gaussianity in Independent Component Analysis. *J Mach Learn Res*. 2003;4:1177–203.
10. Carlet C, Danger JL, Guilley S, Maghrebi H, Prouff E. Achieving side-channel high-order correlation immunity with leakage squeezing. *J Cryptogr Eng*. 2014 Jun 1;4(2):107–21.
11. Rioul O, Cheng W, Guilley S. Cumulant Expansion of Mutual Information for Quantifying Leakage of a Protected Secret. In: 2021 IEEE International Symposium on Information Theory (ISIT). 2021. p. 2596–601.
12. Berg HC, Purcell EM. Physics of chemoreception. *Biophysical Journal*. 1977 Nov 1;20(2):193–219.
13. ten Wolde PR, Becker NB, Ouldridge TE, Mugler A. Fundamental Limits to Cellular Sensing. *J Stat Phys*. 2016 Mar 1;162(5):1395–424.
14. Mora T, Nemenman I. Physical Limit to Concentration Sensing in a Changing Environment. *Phys Rev Lett*. 2019 Nov 5;123(19):198101.
15. Hinczewski M, Thirumalai D. Cellular Signaling Networks Function as Generalized Wiener-Kolmogorov Filters to Suppress Noise. *Phys Rev X*. 2014 Oct 29;4(4):041017.
16. Tjalma AJ, Galstyan V, Goedhart J, Slim L, Becker NB, ten Wolde PR. Trade-offs between cost and information in cellular prediction. *Proceedings of the National Academy of Sciences*. 2023 Oct 10;120(41):e2303078120.
17. Wiener N, Masani P. The prediction theory of multivariate stochastic processes: I. The regularity condition. *Acta Mathematica*. 1957 Jan;98(none):111–50.

18. Bialek W. Biophysics: Searching for Principles [Internet]. Princeton University Press; 2012 [cited 2020 Jun 18]. Available from: <https://press.princeton.edu/books/hardcover/9780691138916/biophysics>
19. Oppenheim A, Verghese G. Signals, Systems and Inference. 1st ed. Pearson; 2016. (Prentice Hall Signal Processing Series).
20. Kalman RE. A New Approach to Linear Filtering and Prediction Problems. *Journal of Basic Engineering*. 1960 Mar 1;82(1):35–45.
21. Kalman RE, Bucy RS. New Results in Linear Filtering and Prediction Theory. *Journal of Basic Engineering*. 1961 Mar 1;83(1):95–108.
22. Keegstra JM, Kamino K, Anquez F, Lazova MD, Emonet T, Shimizu TS. Phenotypic diversity and temporal variability in a bacterial signaling network revealed by single-cell FRET. Barkai N, editor. *eLife*. 2017 Dec 12;6:e27455.
23. Colin R, Rosazza C, Vaknin A, Sourjik V. Multiple sources of slow activity fluctuations in a bacterial chemosensory network. Barkai N, editor. *eLife*. 2017 Dec 12;6:e26796.
24. Yuan J, Branch RW, Hosu BG, Berg HC. Adaptation at the output of the chemotaxis signalling pathway. *Nature*. 2012 Apr;484(7393):233–6.
25. Tostevin F, ten Wolde PR. Mutual Information between Input and Output Trajectories of Biochemical Networks. *Phys Rev Lett*. 2009 May 27;102(21):218101.
26. Wiener N. Extrapolation, Interpolation, and Smoothing of Stationary Time Series: With Engineering Applications. Cambridge, MA, USA: MIT Press; 1949. 163 p.
27. Havlicek JP. Module 4: The Wiener Filter [Internet]. Kalman Filtering. 2005. Available from: <https://coecs.ou.edu/Joseph.P.Havlicek/Kalman/notes/KalmanModule4.pdf>

96. Mattingly HH, Emonet T. Collective behavior and nongenetic inheritance allow bacterial populations to adapt to changing environments. *Proceedings of the National Academy of Sciences*. 2022 Jun 28;119(26):e2117377119.
97. Armstrong JB, Adler J, Dahl MM. Nonchemotactic Mutants of *Escherichia coli*. *Journal of Bacteriology*. 1967;93(1):390–8.
98. Bachmann BJ. Pedigrees of Some Mutant Strains of *Escherichia coli* K-12. 1972;36:33.
99. Barker CS, Prüß BM, Matsumura P. Increased Motility of *Escherichia coli* by Insertion Sequence Element Integration into the Regulatory Region of the *flhD* Operon. *Journal of Bacteriology*. 2004 Nov 15;186(22):7529–37.
100. Briegel A, Ortega DR, Tocheva EI, Wuichet K, Li Z, Chen S, et al. Universal architecture of bacterial chemoreceptor arrays. *Proceedings of the National Academy of Sciences*. 2009 Oct 6;106(40):17181–6.
101. Waite AJ, Frankel NW, Emonet T. Behavioral Variability and Phenotypic Diversity in Bacterial Chemotaxis. *Annual Review of Biophysics*. 2018;47(1):595–616.
102. Li L, Zhang X, Sun Y, Ouyang Q, Tu Y, Luo C. Phenotypic Variability Shapes Bacterial Responses to Opposing Gradients. *PRX Life*. 2024 Jan 9;2(1):013001.
103. Qin D, Xia Y, Whitesides GM. Soft lithography for micro- and nanoscale patterning. *Nature Protocols*. 2010 Mar;5(3):491–502.
104. Edelstein A, Amodaj N, Hoover K, Vale R, Stuurman N. Computer Control of Microscopes Using μ Manager. *Current Protocols in Molecular Biology*. 2010;92(1):14.20.1-14.20.17.
105. Zal T, Gascoigne NRJ. Photobleaching-Corrected FRET Efficiency Imaging of Live Cells. *Biophysical Journal*. 2004 Jun 1;86(6):3923–39.